Deutsches Zentrum
für Luft- und Raumfahrt
German Aerospace Center

University of Stuttgart
Germany

MASTER'S THESIS

Analysis of the performance parameters of Satellite Laser Ranging (SLR) systems based on the link budget under exemplary inclusion of the miniSLR system

Analyse der Leistungsparametern von Satellite Laser Ranging (SLR) Systemen anhand des Link Budgets unter exemplarischer Einbeziehung des miniSLR Systems

by cand. aer. Tristan Meyer
Student ID: 3152065

Reviewer:
Prof. Dr. rer. nat. Thomas Dekorsy
Institute of Aerospace Thermodynamics (ITLR)
University of Stuttgart
and
Institute of Technical Physics
German Aerospace Center (DLR)

Supervisors:
Dr. rer. nat. Daniel Hampf
Institute of Technical Physics
German Aerospace Center (DLR)

Felicitas Niebler
Institute of Technical Physics
German Aerospace Center (DLR)

October, 2022

Eidesstattliche Erklärung

Hiermit erkläre ich mich damit einverstanden, dass meine Masterarbeit zum Thema

> Analysis of the performance parameters of Satellite Laser Ranging (SLR) systems based on the link budget under exemplary inclusion of the miniSLR System

in der Institutsbibliothek des Instituts für Thermodynamik der Luft- und Raumfahrt öffentlich zugänglich aufbewahrt und die Arbeit auf der Institutswebseite sowie im OnlineKatalog der Universitätsbibliothek erfasst wird. Letzteres bedeutet eine dauerhafte, weltweite Sichtbarkeit der bibliographischen Daten der Arbeit (Titel, Autor, Erscheinungsjahr, etc.). Nach Abschluss der Arbeit werde ich zu diesem Zweck meinem Betreuer neben dem Prüfexemplar eine weitere gedruckte sowie eine digitale Fassung übergeben. Der Universität Stuttgart übertrage ich das Eigentum an diesen zusätzlichen Fassungen und räume dem Institut für Thermodynamik der Luft- und Raumfahrt an dieser Arbeit und an den im Rahmen dieser Arbeit von mir erzeugten Arbeitsergebnissen ein kostenloses, zeitlich und örtlich unbeschränktes, einfaches Nutzungsrecht für Zwecke der Forschung und der Lehre ein. Falls in Zusammenhang mit der Arbeit Nutzungsrechtsvereinbarungen des Instituts mit Dritten bestehen, gelten diese Vereinbarungen auch für die im Rahmen dieser Arbeit entstandenen Arbeitsergebnisse.

.....
Ort, Datum, Unterschrift

Hiermit versichere ich, dass ich diese Masterarbeit selbstständig mit Unterstützung des Betreuers angefertigt und keine anderen als die angegebenen Quellen und Hilfsmittel verwendet habe. Die Arbeit oder wesentliche Bestandteile davon sind weder an dieser noch an einer anderen Bildungseinrichtung bereits zur Erlangung eines Abschlusses eingereicht worden. Ich erkläre weiterhin, bei der Erstellung der Arbeit die einschlägigen Bestimmungen zum Urheberschutz fremder Beiträge entsprechend den Regeln guter wissenschaftlicher Praxis eingehalten zu haben. Soweit meine Arbeit fremde Beiträge (z.B. Bilder, Zeichnungen, Textpassagen, etc.) enthält, habe ich diese Beiträge als solche gekennzeichnet (Zitat, Quellangabe) und eventuell erforderlich gewordene Zustimmungen der Urheber zur Nutzung dieser Beiträge in meiner Arbeit eingeholt. Mir ist bekannt, dass ich im Falle einer schuldhaften Verletzung dieser Pflichten die daraus entstehenden Konsequenzen zu tragen habe.

.....
Ort, Datum, Unterschrift

Acknowledgement

I would like to take this opportunity to thank all those who supported me during the preparation of this master's thesis.

First, I would like to thank **Prof. Dr. Thomas Dekorsy** for the opportunity to undertake this thesis and for agreeing to be the reviewer for this work. It has given me a valuable insight into the world of SLR technology and the practical applications of lasers in aerospace.

I thank my supervisors **Dr. Daniel Hampf** and **Felicitas Niebler** for their support on providing specific information and giving me valuable advice.
Special thanks goes to the entire team who kept the miniSLR alive and to enable the inclusion of the miniSLR in this thesis.

I would like to thank **Dr. Nils Bartels**, who gave me interesting insights towards retroreflectors and their applications.

Furthermore, I thank all friends who repeatedly gave me confidence in difficult phases and to consistently pursue my goal.
Finally, I also would like to thank my family for their unfailing support and ongoing encouragement throughout my studies.

Abstract

The network of Satellite Laser Ranging (SLR) is expanding every year, which is partly driven by new applications such as space traffic management as well as new companies that commercialise the technology. For the design of new ground segments, it is important to find the balance between an optimisation of the link budget, e.g., through the utilisation of high-power lasers, large telescopes, etc., and the mass, the volume, and the overall costs of such systems. A key uncertainty in the estimation of the link budget remains the Optical Cross Section (OCS) of the satellites that are equipped with retroreflectors.
In the context of this work, the practical in-orbit OCS from SLR measurements are derived with a given link budget model and evaluated.
The analysis is accomplished using historical SLR measurements provided by the International Laser Ranging Service (ILRS) network and data, which is obtained from conducted measurements with the system developed at the DLR, namely the miniSLR. The measurements of the systems are summarised and a filter algorithm is applied to identify single photon operating stations. Throughout a selection of satellites, the outcomes of individual single photon stations are investigated. It shows that out of the 28 stations providing single photon SLR measurements, only a small number remains that provide reliable and consistent data. Others exhibit a relative systematic error, which indicates that incorrect system specifications might be stated, but also the applied return rate control comprise these errors. The selected stations are then used to derive the in-orbit OCSs.
In addition, theoretical values are determined from a state-of-the-art analytical approach. These are exploited to gain a first validation of the results from the SLR measurements. The theoretical values are prior evaluated against the existing literature values, which were computed via diffraction theory. It shows that the proposed method yields reasonable OCSs for most types of arrays, but can feature larger discrepancies in specific cases.
From the derivations of the link budget it appears that for high orbiting satellites, the discrepancies between the theoretical and the practical values are moderate, which endorses the application of the link budget. For Low Earth Orbit (LEO) satellites the OCSs can differ in a larger manner. The origin to this is not fully clear, but can be presumably attributed to dynamical effects, such as tracking uncertainties. Consequently, the utilised link budget model features some flaws, which may be eliminated in future studies.

Keywords: Satellite Laser Ranging, Retroreflectors, Link Budget

Kurzfassung

Das SLR Netzwerk wird Jahr für Jahr erweitert, was zum Teil auf neue Anwendungen wie das Weltraumverkehrsmanagement, sowie auf neue Unternehmen zurückzuführen ist, die diese Technologie kommerziell nutzen. Bei der Konzeption neuer Bodensegmente ist es wichtig, ein Kompromiss zwischen der Optimierung des Link Budgets, z.B. durch den Einsatz von Hochleistungslasern, großen Teleskopen usw., und der Masse, dem Volumen und den Gesamtkosten solcher Systeme zu finden. Ein wesentlicher Unsicherheitsfaktor bei der Abschätzung des Link Budgets ist nach wie vor die OCS von Satelliten, die mit Retroreflektoren ausgestattet sind.
Im Rahmen dieser Arbeit werden die praktischen in-Orbit OCSs aus SLR-Messungen mit einem gegebenen Link-Budget-Modell abgeleitet und bewertet.
Die Analyse erfolgt unter Verwendung historischer SLR-Messungen, die vom ILRS-Netzwerk zur Verfügung gestellt wurden, und von Daten, die aus durchgeführten Messungen mit dem am DLR entwickelten System, dem miniSLR, gewonnen wurden. Die Messungen der Systeme werden zusammengefasst und ein Filteralgorithmus wird angewandt, um Stationen, welche im single-photon Betrieb arbeiten zu identifizieren. Anhand einer Auswahl von Satelliten werden die Ergebnisse der einzelnen Stationen untersucht. Es zeigt sich, dass von den 28 Stationen, welche single-photon Messungen durchführen, nur eine kleine Anzahl übrig bleibt, die zuverlässige und konsistente Daten liefert. Andere weisen einen relativen systematischen Fehler auf, was darauf hindeutet, dass möglicherweise falsche Systemspezifikationen angegeben werden, aber auch die angewandte Return-Raten-Kontrolle diese Fehler umfasst. Die ausgewählten Stationen werden dann zur Ableitung der in-Orbit OCSs verwendet.
Zusätzlich werden theoretische Werte aus einem modernen analytischen Ansatz ermittelt. Diese werden genutzt, um eine erste Validierung der Ergebnisse der SLR-Messungen vorzunehmen. Die theoretischen Werte werden vorherig mit den bestehenden Literaturwerten verglichen, die mit Hilfe der Beugungstheorie berechnet wurden. Es zeigt sich, dass die vorgeschlagene Methode für die meisten Arten von Arrays vernünftige OCSs liefert, aber in bestimmten Fällen größere Diskrepanzen aufweisen kann.
Aus den Ableitungen des Link Budgets geht hervor, dass die Diskrepanzen zwischen den theoretischen und den praktischen Werten für Satelliten in hoher Umlaufbahn moderat sind, was die Anwendung des Link-Budgets befürwortet. Für LEO-Satelliten können die OCSs in größerem Maße abweichen. Die Ursache hierfür ist nicht ganz klar, kann aber vermutlich auf dynamische Effekte, wie z.B. Nachführunsicherheiten, zurückgeführt werden. Folglich weist das verwendete Link-Budget-Modell einige Schwächen auf, die in zukünftigen Studien beseitigt werden können.

Nomenclature

Abbreviations

CCR	Corner Cube Reflector
CRD	Consolidated Laser Ranging Data
CSPAD	Compensated Single-Photon Avalanche Diode
DLR	Deutsches Zentrum für Luft- und Raumfahrttechnik
ECI	Earth-Centered-Inertial
EDC	EUROLAS Data Center
FFDP	Far-Field Diffraction Pattern
FTP	File Transfer Protocol
GEO	Geostationary Earth Orbit
GNSS	Global Navigation Satellite System
ILRS	International Laser Ranging Service
ITP	Institute of Technical Physics
ITRF	International Terrestrial Reference Frame
LEO	Low Earth Orbit
MCP	Micro-Channel Plate
MEO	Mid Earth Orbit
NaN	Not a Number
ND	Neutral Density
NIR	Near Infrared
NP	Normal Point
OC	Operation Center
OCS	Optical Cross Section
OOOS	Orbital Objects Observation Software
PMT	Photon-Multiplier Tube
SGP	Simplified General Pertubation
SLR	Satellite Laser Ranging
SPAD	Single-Photon Avalanche Diode
TIR	Total Internal Reflection
TLE	Two Line Elements
TOF	Time Of Flight
UROL	Uhlandshoehe Research Observatory

Physical Constants

c	$299{,}792{,}458\,\mathrm{m\,s^{-1}}$	Speed of light in vacuum
h	$6.626{,}070{,}15 \times 10^{-34}\,\mathrm{J\,s^{-1}}$	Planck constant
g	$9.81\,\mathrm{kg\,s^{-2}}$	Earth gravity

Latin Symbols

A	m^2	Aperture
A_r	m^2	Receiver aperture
D	m	Diameter
E_p	J	Pulse energy
f_l	Hz	Laser repetition rate
G_t	sr^{-1}	Transmitter gain
h	m	Altitude
J_1	-	First kind Bessel function
k	-	Number of expected events
N_{bin}	-	Number of range measurements
N_{pe}	-	Number of generated photo electrons per pulse
N_t	-	Number of photons emitted per laser pulse
L	m	Length
lat	°	Station latitude
lon	°	Station longitude
n	-	Refractive index
n_δ	-	Number of dihedral offsets
P_d	-	Detection probability
R	m	Slant range
R_E	m	Earth radius
$\hat{r}$	m	Unit vector from the SLR station to the satellite
$\hat{s}$	m	Unit vector from the center of the Earth to the satellite
T_{bin}	s	Epoch bin
t	s	Time of flight
V	m	Visual range
$\hat{v}$	$m\,s^{-1}$	Unit vector of the satellite's movement in space

Greek Symbols

α	rad	Velocity aberration
α_c	rad	Compensated velocity aberration
α_e	rad	Elevation angle
α_s	rad	Shifted velocity aberration
Γ	-	Quantity
γ	rad	Mean angular distance
γ_t	-	Attenuation coefficient
δ	rad	Dihedral angle offset
η	-	Factor of reduction
η_{obs}	-	Amount of obscuration
η_q	-	Quantum efficiency
θ	rad	Off-axis angle
θ_c	rad	Cut-off angle
θ_d	rad	Far field beam divergence half-angle
θ_i	rad	Incidence angle
θ_i'	rad	Propagation angle

$\Delta\theta_p$	rad	Beam pointing error
λ	m	Wavelength
μ	-	Reduced aperture radius
ρ	-	Reflectivity
σ	$m^2\,sr^{-1}$	Optical cross section
σ_0	$m^2\,sr^{-1}$	Peak cross-section
τ	-	Transmission
τ_{atm}	-	Transmission of the atmosphere
τ_c	-	Transmission of cirrus clouds
τ_i	-	Transmission of all elements
τ_r	-	Transmission efficiency of the receiver
τ_{filter}	-	Filter transmission
τ_t	-	Transmission efficiency of the transmitter
Ω	sr	Effective solid angle
ω	rad	Angle

Indices

atm	Atmosphere
ccr	Corner Cube Reflector
E	Earth
gnss	Global Navigation Satellite System
max	Maximum
min	Minimum
obs	Obscuration
r	Receiver
t	Transmitter
sat	Satellite
zen	Zenith

Contents

1 Introduction

Ruth Stilwell, executive director of Aerospace Policy Solutions, once said during a panel discussion:

> *For right of way, the regulatory framework is please don't crash your satellite, and really please don't crash it into somebody else* [1].

Close approaches are becoming more common in LEO, as the number of satellites increases. SpaceX's Starlink constellation, with nearly 1700 satellites in orbit today, has contributed to many of those, such as one in September 2019 when the European Space Agency said it moved an Earth observation satellite, Aeolus, to avoid a close approach with a Starlink satellite [1]. These events show that space monitoring is becoming increasingly important. One promising way is to utilise SLR, to monitor and predict the satellites orbits. SLR is an established technology to measure distances to satellites equipped with retroreflectors [2]. The current SLR network faces in this manner a few challenges. First of all, the global coverage of SLR stations remains uneven, whereby most of the stations are located on the upper hemisphere [3]. On the other hand, many stations are already at or beyond their limit in terms of tracking requests [2].
Consequently, the current SLR network has to be expanded and the technology has to become more accessible, in order to meet the growing demand of objects to be tracked. One major problem in to dates legacy systems is that these comprise of large observatories and thus require elaborate infrastructure, are expensive and mostly require on-site staff for operation. This leads to the need for small, inexpensive and autonomous systems that can be transported and placed anywhere on the globe.

In order to construct the system as small as possible, they should only contain the necessary elements. Accordingly, the power and hardware is limited. Powerful lasers and large telescopes require a lot of space and energy. The systems must therefore be optimised for the application and performance. In order to gain insight of a systems performance, link budgets are employed. These determine the detectable signal for a given system, which enables its evaluation and validation. The link budget depends on several system specifications, such as the laser energy, the telescope diameter or the detector efficiency, but also on the space segment, i.e. the orbit height and the utilised retroreflectors [4].
However, since the need for compact ground segments is emerging, it is important to find the balance between an optimisation of the link budget, e.g., through the utilisation of high-power lasers, large telescopes, etc., and the mass, the volume, and the overall costs of such systems. A key uncertainty in the estimation of the link budget remains the OCS of the satellites that are equipped with retroreflectors.
The OCS is to date a rare parameter. It describes the amount of signal that is reflected back to the source, i.e., the ground station and is therefore essential for the signal estimation. Arnold [5] and Degnan [4, 6] extensively studied and advanced the mathematics of retroreflectors, and thus computed OCSs for several satellites. But with the vast growing utilisation of retroreflectors on newly launched satellites, especially Global Navigation Satellite

System (GNSS) satellites, these values are to date barely available. In particular for the wavelength of 1064 nm values are scarcely available, since 532 nm is the most common ranging wavelength. Therefore, making the signal estimation via the link budget more difficult for the former mentioned wavelength.

This study addresses the goal to derive the in-orbit OCSs from obtained SLR measurements, in order to expand the state of the literature values, and to provide OCSs for the wavelength of 1064 nm. Pursuing the goal that these obtained values can in future be used for link budget estimations, for newly launched satellites. Besides the data provided by the ILRS network, contributing to the analysis, further the over the past few years developed miniSLR system of the DLR in Stuttgart, Germany, which operates at a wavelength of 1064 nm provides valuable measurements.

This work makes use of the analytical link budget model derived by Degnan [4].
In contrast, a simplified model for the theoretical calculation of the OCS is employed. This model was derived by Degnan [6], which is based on the derivations of Arnold [5]. Exemplary theoretically obtained values shall serve as a first reference for the evaluation and validation of the values obtained from the SLR measurements. Previously, the self-calculated values are evaluated against existing literature values.

This thesis is divided into the following chapters: First, the theory relevant to this project is discussed and the utilised link budget model is explained. Furthermore, the properties of retroreflectors are summarised and Degnan's simplified model is presented and explained in detail. Following, the data collection is outlined in Chapter 3. In addition, the theoretical values obtained in this process are discussed. An essential part of this thesis is the processing of the data and the derivation of the OCS from the SLR measurements, which is explained in Chapter 4.
Chapter 5 discusses the main results. In this manner the findings of the individual contributing stations is discussed and evaluated. Moreover, the OCSs derived from the link budget are discussed and compared to the theoretical values. The last chapter summarises the content of this thesis and gives an overview of the obtained results. At the end, possible additions and improvements to the method are discussed.

2 Satellite Laser Ranging

The idea of measuring the range of a satellite in orbit around Earth was pioneered in the early 1960s. The first successful ranging experiment was reported in 1964 which tracked the Beacon-B (also known as Explorer-22) satellite for ten successful flyovers in the period of three days [7, p. 302]. In the early stages SLR contributed to studies in tectonic plate motion, crustal deformation, Earth orientation, the Earth's gravity field. However, these early experiments achieved only an accuracy of several meters [8, 3].
In the years that followed, many satellites were launched carrying retroreflector targets. Furthermore, a global network of SLR stations was established and improved technologies brought greater accuracy, precision and capability. Today, the SLR network continues to maintain the International Terrestrial Reference Frame (ITRF) and to support Earth observation satellites, including altimetry missions, through precise orbit determination and validation [3]. Whereby, today's stations can determine the distance to a target with millimetre accuracy [7].

A major aspect in the development of a SLR station is the determination of the expected signal strength, which, in turn, determines the utilised hardware. A large part of this work comprises the link budget which is outlined in detail in Chapter 2.3. Then, a brief insight in detectors and their respective detection probability is given. Lastly, in Chapter 3.2.1, the basic principles of retroreflectors as well as their significance with regard to the link budget are described. A method proposed by Degnan [6] for the theoretical calculating of the OCS completes the prerequisites of this work.

2.1 Principles of satellite laser ranging

The fundamental observable in satellite laser ranging is the measurement of the round-trip flight time of a laser pulse [8]. For this, a laser pulse is emitted by a laser transmitter of a ground segment and is fired at a satellite. The departing laser pulse triggers an event timer at a certain time. In order to obtain these measurements along a full orbit arc, the satellite needs to be tracked. This is accomplished either by optical systems or by orbit predictions. The satellite is equipped with special reflectors, called retroreflectors, that reflect the incident light back to its source. These reflectors make up the space segment of SLR and are passive components, which do not require any interface to the satellite bus. The reflected laser pulse is then registered by light-detecting devices of the SLR ground segment and converted into a voltage. Thereby, the detector emits a stop signal to be sent to the event timer. As a result, the Time Of Flight (TOF) of the laser beam is determined, which comprises the two-way time of the pulse. The range R to the target results from half the TOF multiplied by the speed of light c:

$$R = \frac{c \cdot TOF}{2}. \tag{2.1}$$

The speed of light is in fact not constant along the TOF and is reduced by the refractive

index of the medium. This effect needs to be taken into account in order to resolve the distance to the target as precises as possible.
Transmitting and recording several laser pulses as the satellite travels over the SLR station, an orbital arc is obtained. This allows orbital modelling calculations to infer the entire orbital ephemeris. If this is combined with measurements from other stations, a highly accurate orbital determination can be produced.

2.2 The miniSLR system

The miniSLR follows the concept of a minimal SLR station, consisting only of the necessary components and occupying minimal space, without ranking behind regular SLR segments [9]. Making SLR a more accessible and affordable concept. If retroreflectors on satellites become more common, a small network of standardised miniSLR systems around the world could provide extremely accurate orbital data at very competitive costs [10].
The system is placed on top of the roof of the Institute of Technical Physics (ITP) in Stuttgart, Germany (see Figure 2.1) , with the geodetic coordinates 48.7489°N, 9.1026°O.

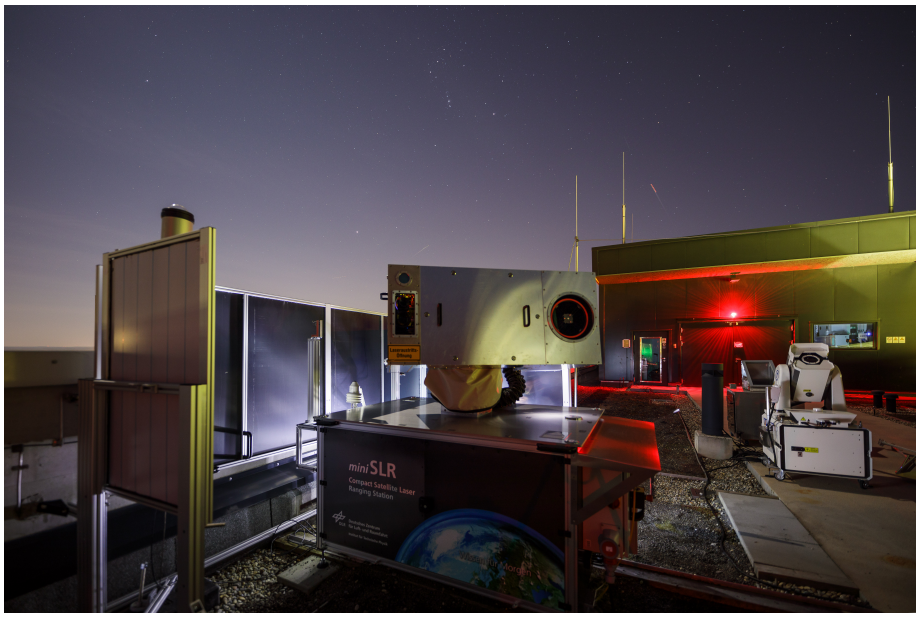

Figure 2.1: View of the miniSLR system, placed on the roof of the DLR in Stuttgart, Germany. (Photo: Paul Wagner / DLR)

It contains all of the optics and electronics within a small footprint of 2.3 m x 1.3 m x 2.0 m. The controlling electronics are stored in a lower compartment, whereas a top compartment encloses the optical components, such as the receiving telescope and the laser head. Due to its small aperture, the miniSLR makes use of a high repetitive and high pulse energy laser source to compensate the loss on the receiver side [9]. In order to track a satellite, the top compartment can be rotated in a full hemisphere around two axes, conducted by an altitude-azimuth telescope mount. Light received by the telescope is coupled into a multi-mode fibre and detected by a single photon counting device.
The compartments are fully sealed and air conditioned, thus maintaining stable conditions, which are relevant for the precision of the system.

Moreover, the system is operated via the in-house developed Orbital Objects Observation Software (OOOS). The software utilises a user-friendly interface and is designed to take over all tasks related to the operation of a SLR segment. This includes the real-time operation, such as the scheduling, tracking and ranging and the control of the infrastructure, e.g., the laser. In addition, OOOS enables the experimental evaluation of the obtained data. Furthermore, it offers the potential to operate the system in a high degree, up to full automation [11]. In the long term, the miniSLR system shall operate fully autonomous, which has been partially proven to date.

2.3 The link budget equation

In order to evaluate the performance of a SLR system, the link budget is applied. It derives the returned signal strength, which is declared as the detected photoelectrons per yielded laser pulse. It depends on the system itself and thus the hardware specifications, but also the space segment contributes to the received signal. Additionally, environmental and orbital geometries determine the signal strength. This metric allows system designers to determine an estimate if the average signal strength is lower than the noise or detection threshold of the electronics. If so, then it will not be possible to detect a return from a satellite.
The theory of SLR measurements and the link budget has been extensively studied by Degnan [4] whose work forms the basis for the calculations that are presented in this thesis. This section presents the link budget equation and the corresponding parameters. Those parameters comprise characteristics of both the ground segment and the space segment.

The adapted radar link equation represents the use of laser ranging and is given by

$$N_{pe} = N_t \cdot G_t \cdot \left(\frac{1}{4 \cdot \pi \cdot R^2}\right)^2 \cdot \sigma \cdot A_r \cdot \tau_r \cdot \tau_t \cdot \eta_q \cdot \tau_{filter} \cdot \tau_{atm}^2 \cdot \tau_c^2. \tag{2.2}$$

The equation calculates the mean number of photo electrons N_{pe} which are recorded by the detector of the ground segment per emitted laser pulse. It depends on the number of photons emitted per laser pulse N_t, the transmitter gain G_t, the slant range R, the optical cross section σ, the receiver aperture A_r, the transmission efficiency of the receiver τ_r, the transmission efficiency of the transmitter τ_t, the quantum efficiency η_q, the filter transmission τ_{filter}, and the transmission of the atmosphere τ_{atm} [4].

Emitted photons of laser N_t

The first quantity on the right side of the equation is the number of photons N_t that is emitted per laser pulse. It is calculated by

$$N_t = \frac{E_p \cdot \lambda}{h \cdot c}, \tag{2.3}$$

where N_t is a function of the pulse energy E_p, the wavelength λ of the laser, the Planck constant h, and the speed of light in vacuum c [4].

Transmitter gain G_t

The transmitter gain G_t for a Gaussian beam is given by

$$G_t = \frac{8}{\theta_d^2} \cdot \exp\left[-2\left(\frac{\Delta\theta_p}{\theta_d}\right)^2\right]. \tag{2.4}$$

Here, θ_d is the far field beam divergence half angle between the beam centre and the $1/e^2$ intensity point. The exponential term is denoted by the static beam pointing loss. It depends on $\Delta\theta_p$, which is the resulting beam pointing error from the centre of the beam [4].

Slant range R

The slant range, i.e., the distance between a ground segment and an object in space is calculated by the geometric coherence. It is given by

$$\begin{aligned} R = &-(R_E + h_{station}) \cdot \cos\left(\frac{\pi}{2} - \alpha_e\right) \\ &+\sqrt{\left[(R_E + h_{station}) \cdot \cos\left(\frac{\pi}{2} - \alpha_e\right)\right]^2 + 2R_E(h_{sat} - h_{station}) + h_{sat}^2 - h_{station}^2}. \end{aligned} \tag{2.5}$$

This equation comprises the Earth radius R_E, the station altitude above sea level $h_{station}$, the satellite altitude above sea level h_{sat}, and the elevation angle α_e. The elevation angle describes the angle between the horizontal plane and the line of sight, i.e., the emitted laser beam [4].

Optical cross section σ

Next, σ denotes the Optical Cross Section (OCS) of a single retroreflector or a retroreflector array, which is mounted onto the satellite. It defines the amount of light that is reflected back to the ground segment. This quantity is a complex function of the retroreflector properties, including the material, the coating, the dihedral offset angle, the aperture size, and the form of the array. Other factors of relevance are the orientation, the spatial distribution, and the incident light. The OCS and an appropriate, analytical method of calculation are described in more detail in Chapter 2.5. Since this property depends on several influences, such as the angle of incidence and the position of the satellite with respect to the ground station, a common method is to derive an average value along multiple angles of incident and the velocity aberration annulus.

Receiver aperture A_r

The term A_r describes the effective receiver aperture area that is seen by the reflected beam and is given by

$$A_r = \frac{\pi}{4} \cdot D_r^2 \cdot (1 - \eta_{obs}). \tag{2.6}$$

It depends on the receiving optical system with a diameter D_r of the main receiving optics as well as the amount of obscuration η_{obs} due to a secondary mirror.

Transmission of optics and quantum efficiency

The parameters τ_r and τ_t represent the total transmission efficiency of the receiver and transmitter optics, respectively. They are the products of the transmission of all elements τ_i in the beam path according to

$$\tau_{r,t} = \prod_{i}^{n} \tau_i. \tag{2.7}$$

To reduce the noise originating from the background radiation during daylight observations, bandpass filters are implemented into the receiver path. These transmit the light of a particular wavelength in a given range. However, this method is associated with transmission losses τ_{filter}.
The quantum efficiency η_q describes the effectiveness of the detector that converts an incident photon into an electron. This conversion factor depends on the wavelength of the incident light.

Atmospheric transmission τ_{atm} and τ_c

The term τ_{atm} describes the one-way atmospheric transmission of the laser beam propagating the Earth's atmosphere. The attenuation of light in the visible and the infrared wavelength occurs due to the absorption and the scattering, which is caused by air molecules, solid, and liquid particles. The latter ones are aerosols, consisting of dust, haze, and fog [12].
To take these effects into account, an atmospheric transmission was proposed [4]. It is based on the Lambert-Beer law [13] and assumes a straight line path between the observing station and the object being observed, i.e., it ignores the refractive bending of the ray in the atmosphere [4]. This assumption leads to

$$\tau_{atm}(\lambda, V) = \exp\left[-\frac{\gamma_t(\lambda, V, 0) h_{scale}}{\cos\left(\frac{\pi}{2} - \alpha_e\right)} \exp\left(-\frac{h_{station}}{h_{scale}}\right)\right]. \tag{2.8}$$

In general, the total attenuation coefficient γ_t in Equation 2.8 decreases approximately exponentially with the height. It is given by

$$\gamma_t(\lambda, h, V) = \gamma_t(\lambda, 0, V) \cdot \exp\left[-\frac{h}{h_{scale}}\right], \tag{2.9}$$

where $\gamma_t(\lambda, 0, V)$ is the attenuation coefficient at sea level and h_{scale} is a scale height with a value of 1.2 km.
A semi-empirical model, the so-called Kruse model, is commonly used in SLR to obtain the attenuation coefficient at sea level height [13]. The named model yields

$$\gamma_t(\lambda, 0, V) = \frac{3.912}{V[km]} \cdot \left(\frac{\lambda[nm]}{550}\right)^{-q}. \tag{2.10}$$

It depends on the visual range V that is defined as the distance at which the contrast of a black object at daylight compared to the horizon reaches a threshold of 2 % [14]. Table 2.1 provides the relation of different visibilities and the corresponding weather conditions.

Table 2.1: Various visibilities and the corresponding weather conditions according to [15]

Visibility in km	Weather condition
0 - 0.5	Moderate fog
0.5 - 1	Light fog
1 - 2	Thin fog
2 - 4	Haze
4 - 5	Light haze
10 - 20	Clear
20 - 50	Very clear
>50	Exceptionally clear

The exponent q depends on the particle size distribution and thus on the visible range and is given as

$$q = \begin{cases} 1.6 & \text{for V} > 50\,\text{km} \\ 1.3 & \text{for } 6\,\text{km} < \text{V} < 50\,\text{km} \\ 0.585 \cdot V^{1/3} & \text{for V} < 6\,\text{km} \end{cases} \tag{2.11}$$

[13].
Further atmospheric losses occur due to the presence of cirrus clouds. These are sub-visible clouds that are overhead 50 % of the time at most locations [4] and thus attenuate the signal strength. A global study was conducted by Hall et al. regarding the time cirrus clouds are present at a given location and the thickness of the clouds. The findings show that 75 % of the time the transmission derived from the mean cloud thickness is above a value 0.8, independent of the utilised wavelength [4]. From this insight, the cirrus cloud transmission τ_c is assumed to be 0.8.

Further uncertainties and losses, such as noise from background radiation and atmospheric turbulence can influence the signal strength. These are further discussed by Degnan in [4], but not included in this thesis due to the lack of information and in order to generalise the model for multiple stations around the world. Today's SLR stations reduce noise by the utilisation of spectral and spatial filters. Furthermore, the stations utilise gated detectors, which causes the detector to be switched for the period of time during which a signal is expected. From the aforementioned noise reduction measures, it is assumed that the background noise is negligible.

2.4 Photon detection statistics

The received signal of a transmitted pulse is in general detected by a light sensitive detector, which in addition triggers the stop signal for the TOF determination. SLR stations can be distinguished in two modes of operation. The mode of operation refers to the intensity of the returned laser pulses which are to be detected. Multi photon mode is present when the detection of a yielded laser pulse contains several photons. The counterpart, so-called single photon ranging, is present when the intensity of the returned pulses is limited so that no more than an individual photon should generate a detected photoelectron [16]. The achieved mode is highly dependent on the utilised hardware, but also the target, which is ranged.

SLR stations employ typically three different detector types [17]:

- Single-Photon Avalanche Diode (SPAD) or Compensated Single-Photon Avalanche Diode (CSPAD)
- Micro-Channel Plate (MCP)
- Photon-Multiplier Tube (PMT)

SPAD detectors detect up to a single photon per fired laser pulse. These are however subject to first photon arrival. Meaning, when the return energy exceeds the single photon level, the detected epoch time is being shifted towards earlier epochs, which is also called time walk. CSPAD detectors are an improved version of the SPAD detectors, which can register single to a thousands of photons [17]. They are characterised by compensating for time walk when receiving multi photons. However, single photon detectors can only record a single event for each transmitted laser pulse, which means that the detector may also register background noise or daylight signal as an observation [17]. Another way of conducting bias free range measurements when multi photons are present, is to utilise certain multi photon detectors. These comprise MCP and PMT detectors and are capable of recording multiple returns [18].

2.4.1 Poisson statistics

The rate of detection, i.e., the intensity of the returned signal, can be estimated via a Poisson process, by a simple count of the successful detections for a period of time. The probability distribution for a Poisson process is given by

$$P_d(N_{pe}, k) = \frac{N_{pe}^k \cdot e^{-N_{pe}}}{k!}, \tag{2.12}$$

where k is the number of expected events and N_{pe} is the mean number of generated photoelectrons per pulse, previously defined in Equation 2.3 [16]. Today‘s SLR systems are based on threshold detection. The probability of detection is therefore equal to the probability that the number of photoelectrons detected exceeds the threshold value N_{tr},

$$P_d(N_{pe}, N_{tr}, k) = 1 - e^{-N_{pe}} \sum_{k=0}^{k=N_{tr}-1} \frac{N_{pe}^k}{k!} \tag{2.13}$$

[4]. For multi photon operating systems the threshold N_{tr} is unknown and therefore likewise the distribution. By setting the threshold to one, which is valid for single photon operating systems, the Poisson distribution becomes

$$P_d(N_{pe}) = 1 - e^{-N_{pe}}, \tag{2.14}$$

which is why only single photon systems are considered in this work. At high mean photoelectrons per pulse, P_d tends towards one. But at low mean photoelectrons per pulse, the detection probability resolves to $P_d \approx N_{pe}$[19]. Stations that operate solely in single photon mode, feature return rates below 15 % [17]. Further, they may also limit the returned signal to maintain at single photon levels independent of the ranging conditions. The single photon threshold of 15 % is not a static value, nor consistent and may differ in other literature, such as in [18], which recommends a value of 10 %. This is especially

relevant for SPAD type detectors, to minimise the effect of time walk. Nevertheless, it is assumed in this work that stations utilising multi photon detectors operating below the threshold also remain at single photon levels.

2.4.2 Normal point generation

In general, SLR stations record the time or the distance residuals between measurements and an orbit prediction. Orbit predictions either stem from radar or laser ranging data. In general, the latter is more precise. Before the data is published, a filtering method must be applied to remove false detection and noise. This enables the extraction of the satellites track from the raw data. A common filtering algorithm that is utilised, is the iterative n-sigma filter, which is recommended by the ILRS [20].
After filtering, the data contain information of an orbit segment along with the TOFs of the individual data points. The filtered raw data is also referred to as full rate data. Since observations can last several minutes, a large amount of ranging points are acquired during this time. This is enhanced by the usage of kHz repetition lasers and fast responding detectors. This leads to a vast amount of full rate data for observations.
In order to achieve a reduction of data, so-called Normal Points (NPs) are formed. Therefore, the full rate data points are averaged within selected epoch bins, i.e., orbit segments. They constitute fixed time frames, i.e., normal point bins of an orbit segment and have a dependence on the orbit altitude. These time frames can range from a few seconds for LEO satellites up to several minutes for Geostationary Earth Orbit (GEO) satellites. The ILRS created a recommendation for normal point bins, which can be found on the ILRS webpage [21]. A detailed discussion of the NP algorithm is beyond the scope of this thesis. Additional literature with more information regarding the normal point algorithm can be found on the ILRS webpage [22].
An example of the NP generation from the raw ranging data is presented in Figure 2.2. This example shows the raw residuals of the satellite Lageos-1, which was observed with the miniSLR system. The blue dots indicate the raw data points that were recorded by the detector with no filtering applied. The green dots mark the data points after filtering, i.e., the full rate data and the crosses mark the NP of each epoch bin.

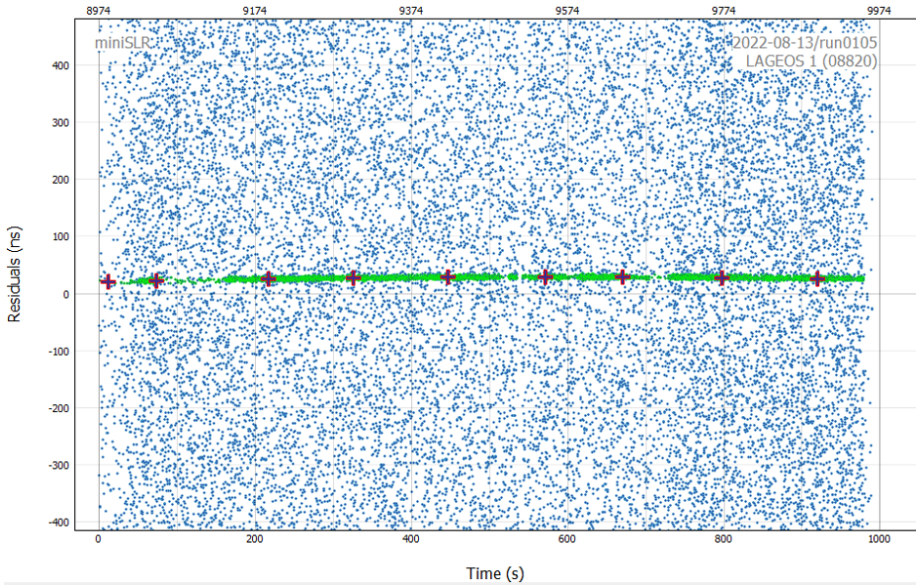

Figure 2.2: Raw residuals (blue dots) versus the observation time from an observation with the miniSLR, ranging Lageos-1 on the 13-08-2022. Green dots mark the filtered data (full rate data), whereas the crosses indicate the average data, i.e., the normal points.

Taking the detection probability into account, the number of range measurements N_{bin} that contribute to a normal point is calculated by

$$N_{bin} = P_d(N_{pe}) \cdot f_l \cdot T_{bin} = (1 - e^{-N_{pe}}) \cdot f_l \cdot T_{bin}. \tag{2.15}$$

The parameter N_{bin} is thus proportional to the detection probability $P_d(N_{pe})$, the laser repetition rate f_l, and the epoch bin T_{bin} [19]. A further common metric to describe the performance is the return frequency, which is the return rate multiplied by the repetition rate of the laser ($P_d \cdot f_l$).

2.5 Retroreflectors and optical cross section

Turning now to retroreflectors, which are small mirror-like devices that are essential for SLR. They retroreflect an incident laser beam straight back along the incident path, irrespective of the angle of incidence [23]. Due to this property, they limit the need for high power lasers, large telescopes, etc. In SLR, the most broadly applied retroreflectors are Corner Cube Reflectors (CCRs), particularly solid CCRs. A solid CCR is a tetrahedron , which consists of three mutually perpendicular reflecting faces and one front face. An example of a CCR is given in Figure 2.3.

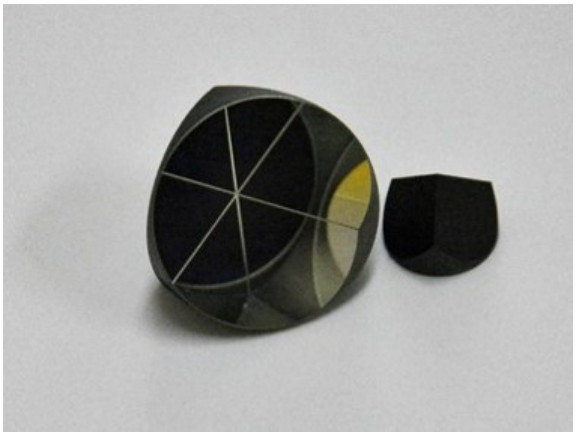

Figure 2.3: Example of a coated solid CCR from [24].

This section describes an analytical state-of-the art approach to derive the theoretical OCS of retroreflectors in SLR. The approach is based on the derivations from Degnan [4, 6] and Stephenson [25].

2.5.1 Common utilised arrays

Before moving on to the calculation, some commonly utilised CCR arrays are presented, which are shown in Figure 2.4. The figure displays the arrays utilised by Lageos-1, Champ and Galileo-1 (left to right). Depending on the orbit altitude and usage, the array features different requirements. Satellites solely exploited for space geodesy are commonly designed as a sphere (Lageos-1). LEO satellites on the other hand do not require large CCRs due to their low altitude and therefore comprise hemispherical arrays with a small number of CCRs. Consequently, only one CCR is illuminated by the SLR beam in general (see Champ). GNSS satellites on the other hand require due to their large distance to the ground segment large arrays that comprise up to one hundred CCRs or more, in order to yield a strong returned signal, as can be seen for Galileo-1.

Figure 2.4: Examples of utilised CCR arrays in SLR. Left: Lageos-1, middle: Champ, right: Galileo-1. Images taken from ILRS webpage [20].

2.5.2 Deriving the optical cross section

The quantitative, OCS (σ) has already been introduced in Chapter 2.3. The OCS is intrinsic to a CCR. The OCS is derived from the Far-Field Diffraction Patterns (FFDPs), which is the spatial and intensity distribution of light that is returned to a laser source from

an illuminated CCR under Fraunhofer conditions. The distance from the source to the CCR is much greater than the aperture diameter. In theory, a perfectly reflecting circular surface that is illuminated at a normal incidence has a FFDP, which can be described by the two-dimensional Airy function [26]. This is the key principle of this approach. In practice the FFDP is derived from ray tracing computations and optical measurements. The following paragraphs show the proposed analytical method for the estimation of the OCS of CCRs with only few input parameters. It should be noted that this method does not account for the following effects:

1) Polarisation dependencies: A beam of light retroreflected from a CCR undergoes two refractions and three reflections. Each encounter introducing a change in either the amplitude or the phase or both. The FFDP is affected by both, whereas the changes in amplitude reduce the the apparent active reflecting area [5].

2) Leaking of uncoated reflectors: Uncoated CCRs rely on Total Internal Reflection (TIR). TIR occurs if the angle of incidence is greater than a certain limiting angle, which depends on the refractive index. This leads to the effect that uncoated CCRs do not reflect light below the limiting angle, which is additionally dependent on the azimuth angle of incidence [5].

3) Uncoated CCRs naturally split the beam into several lobes, offsetting each maximum from the centre of the CCR, affecting the resulting FFDP.

4) Variation of the FFDP dependent on the azimuth angle

5) Clocking of planar arrays, i.e, orientating the CCRs in a different manner to each other

Therefore, this method only constitutes an upper limit for the OCS.

Peak cross section σ_0

The greatest value of the OCS, namely the peak cross section σ_0, is achieved when the CCR is oriented normal to the incident light. The corresponding OCS σ_0 is defined by

$$\sigma_0 = \rho A_{ccr} \left(\frac{4\pi}{\Omega} \right) = \rho \left(\frac{4\pi A_{ccr}^2}{\lambda^2} \right) = \frac{\pi^3 \rho D_{ccr}^4}{4\lambda^2}, \tag{2.16}$$

where ρ denotes the reflectivity of the CCR, A_{ccr} the collecting aperture of the circular cube corner, D_{ccr} the cube diameter, and $4\pi/\Omega$ the on-axis reflector gain and Ω is the effective solid angle occupied by the FFDP of the retroreflector [6].
If the CCR is an uncoated TIR CCR, the peak cross section σ_0 is reduced by the factor of four due to polarisation influences [6].

Far-Filed-Diffraction-Pattern

For a circular aperture, the FFDP of the reflected wave is the Airy Function given by

$$\sigma(\theta) = \sigma_0 \left[\frac{2J_1(x(\theta))}{x(\theta))} \right]^2. \tag{2.17}$$

The Bessel function J_1 is of order one and requires the argument $x(\theta)$, which is calculated by

$$x(\theta) = \frac{\pi D}{\lambda} \sin(\theta), \tag{2.18}$$

The argument x is a function of the off-axis angle θ [6] from the FFDP. For better readability, the notation of the dependency in x on θ is dropped as x is the only variable which depends on θ.

Influence of the incidence angle

Due to variations of the attitude or the spinning of the satellite, the axis normal to the front face of the reflector does not always coincide with the emitted laser beam. Moreover, the orbit propagation of a nadir looking satellite causes a change in the incidence angle (referred to as θ_i) between the normal axis to the front face and the laser beam. A rotation of the retroreflector by the angle θ_i around one axis will contract the apparent width of input and output apertures along the other direction. This effectively turns the shape of the aperture, as it is seen by the laser beam, into the shape of intersecting ellipses [27].
For incident light that is not orientated normal to the CCR, the reflector area A_{ccr} is reduced by the factor $\eta(\theta_i)$. The factor of reduction is given by

$$\eta(\theta_i) = \frac{2}{\pi} \left(\arcsin(\mu) - \sqrt{2}\mu \tan(\theta_i') \right) \cos(\theta_i), \tag{2.19}$$

where θ_i' is the propagation angle inside the solid retroreflector [6]. It is related to the refractive index n and the incidence angle θ_i via Snell's law

$$\theta_i' = \arcsin\left(\frac{\sin(\theta_i)}{n} \right). \tag{2.20}$$

The normalised, reduced aperture radius along the tilt direction is then calculated by

$$\mu = \sqrt{1 - \tan(\theta_i')^2}. \tag{2.21}$$

This reduced (on-axis) peak cross-section becomes a function of the incidence angle, given by

$$\sigma_0(\theta_i) = \eta^2(\theta_i) \cdot \sigma_0 \tag{2.22}$$

[6], and sets the argument x of the Bessel function to

$$x(\theta_i) = \frac{\pi D \eta(\theta_i)}{\lambda} \sin(\theta) \tag{2.23}$$

[6]. Consequently, the above-introduced Equation 2.19 to Equation 2.23 yield

$$\sigma(\theta, \theta_i) = \eta^2(\theta_i)\sigma_0 \left[\frac{2J_1(x(\theta_i))}{x(\theta_i))} \right]^2. \tag{2.24}$$

This provides a re-formulation of Equation 2.17, which is a function of the incidence angle θ_i.

Velocity aberration

The velocity aberration between the satellite and the ground station causes an angular deflection of the reflected beam. In Figure 2.5a this deflection, which is directed in the forward direction of the satellite, is sketched. The velocity aberration angle α can be expressed by

$$\alpha(h_{sat}, \theta_{zen}, \omega) = \alpha_m(h_{sat}) \cdot \sqrt{\cos(\omega)^2 + \Gamma^2(h_{sat}, \theta_{zen}) \cdot \sin(\omega)^2}, \tag{2.25}$$

where θ_{zen} is the transmitter pointing angle from the zenith, and h_{sat} is the satellite height above sea level [6], [25]. The zenith angle θ_{zen} is the complementary angle of α_e. The maximum value is then determined by

$$\alpha_m(h_{sat}) = \frac{2}{c}\sqrt{\frac{R_E^2 g}{R_E + h_{sat}}}, \tag{2.26}$$

where $R_E \approx 6378\,\mathrm{km}$ is the Earth radius and $g = 9.81\,\mathrm{m\,s^{-2}}$ is the surface gravity acceleration of the Earth.
The quantity $\Gamma^2(h_{sat}, \theta_{zen})$ is defined by [6]

$$\Gamma^2(h_{sat}, \theta_{zen}) = 1 - \left(\frac{R_E \cdot \sin(\theta_{zen})}{R_E + h_{sat}}\right)^2 < 1. \tag{2.27}$$

The angle ω depends on the satellite's movement with respect to the SLR station and is calculated from the unit vectors $\hat{s}$, $\hat{r}$, and $\hat{v}$. The corresponding geometrical relation is

$$\omega = \arccos\left[(\hat{s} \times \hat{r}) \cdot \hat{v}\right]. \tag{2.28}$$

The unit vectors represent the following directions:

- $\hat{s}$: from the centre of the Earth to the satellite,
- $\hat{r}$: from the SLR station to the satellite,
- $\hat{v}$: velocity vector of the satellite's movement in space [27], [6].

In consequence, for a given height h_{sat} and zenith angle θ_{zen}, the velocity aberration angle can yield values in the range of

$$\alpha_{max}(h_{sat}) = \alpha(h_{sat}, \theta_{zen}, \omega = 0) = \alpha_m(h_{sat}) \tag{2.29}$$

$$\alpha_{min}(h_{sat}, \theta_{zen}) = \alpha(h_{sat}, \theta_{zen}, \omega = \pi/2) = \alpha_m(h_{sat}) \cdot \Gamma(h_{sat}, \theta_{zen}), \tag{2.30}$$

leading to $\alpha_{max}(h_{sat}) \leq \alpha \leq \alpha_{min}(h_{sat}, \theta_{zen})$ [6].
In Figure 2.5b, the minimal and maximal values of α as a function of the satellite altitude are shown. The maximum zenith angle θ_{zen} is set to 70° for the minimal value of α_{min}, wherefore it is assumed that most SLR stations do not range below an elevation angle of 20°.

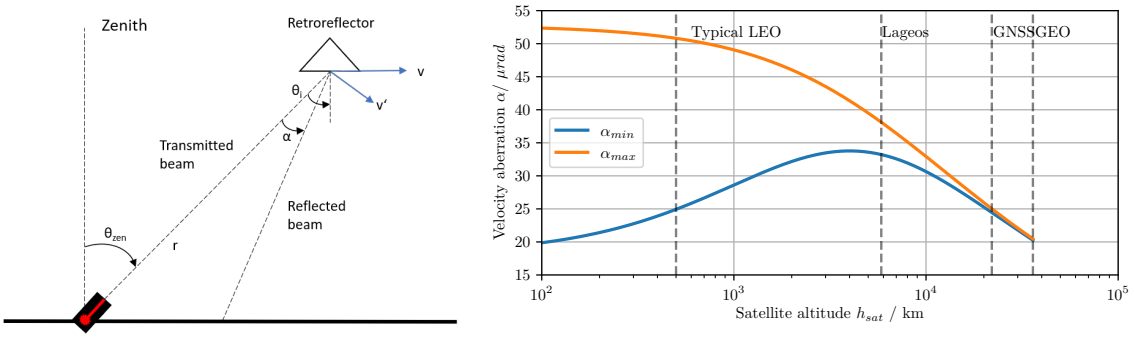

(a) Velocity aberration α causes the reflected beam to be deflected from the origin due to relative velocity v' between satellite and ground station. The incidence angle θ_i reduces the effective area of the CCR.

(b) Minimal and maximal velocity aberration angle α as a function of the satellite altitude above sea level h_{sat}, whereas $\theta_{zen} = 70°$ for α_{min}. Additionally, indicating various satellite types and orbits and their corresponding velocity aberration range.

Figure 2.5

In Figure 2.5b two characteristics of the velocity aberration become obvious. Firstly, the range of the velocity aberration is is highly depended on the satellites altitude. Secondly, it is non-zero for geostationary satellites. The angular velocities around the Earth's rotation axis are the same for a ground station and a geostationary satellite. Nevertheless, the physical velocities are different, which results in a relative velocity between them and therefore a velocity aberration of approximately $20''$.

Spoiling of retroreflectors

The above-mentioned deflection of the beam centre causes the signal to be reduced or to fall into a zero section. A compensation for the velocity aberration and thus an improvement of the signal can be achieved through the application of spoiling in CCRs. Spoiling offsets one or more (n_δ=1 to 3) perfect cube angles from 90° by the dihedral angle δ, which splits the central lobe into $2n_\delta$ spots. This shifts the velocity aberration annulus to the desired main lobe.
The shift of the lobe with respect to the centre of the original airy is expressed with the mean angular distance γ and calculated by

$$\gamma = \begin{cases} \frac{4}{3} \cdot \sqrt{6} \cdot \delta & \text{for } n_\delta{=}3 \\ \frac{2}{3} \cdot \sqrt{6} \cdot \delta & \text{for } n_\delta{=}1 \end{cases} \tag{2.31}$$

[6]. As a counterpart this method reduces the on-axis peak-cross-section of each lobe by

$$\sigma_{0,spoiled} = \frac{\sigma_0}{(2n_\delta)^2}. \tag{2.32}$$

When spoiling is applied, the mean angular displacement of the lobes from the centre compensates for the velocity aberration such that γ shifts the annulus, which is defined by the velocity aberration to the peak or close to the peak of the formed lobes. This is given by

$$\alpha_s = \alpha - \gamma, \tag{2.33}$$

where α_s is the shifted velocity aberration due to spoiling. If no spoiling is present, the relation $\alpha_s = \alpha$ applies.

Maximum incidence angle

CCRs reflect light up to a certain angle, above which reflection is no longer possible. This maximum incidence angle is also referred to as the cut-off angle θ_c and is calculated by

$$\theta_c = \arcsin\left(n \sin\left(\arctan\left(\frac{D_{ccr}}{2L_{ccr}}\right)\right)\right). \tag{2.34}$$

It is a function of the depth of the CCR L_{ccr} and the refractive index n [5]. It is assumed that Equation 2.34 applies for LEO and spherical satellites. In both cases the orientation of the CCR with respect to the incident beam is unknown.
Typical maximal incidence angles for fused silica CCRs ($n \approx 1.46$ for $\lambda = 532\,\text{nm}$) are roughly $\theta_{i,max} \approx 57°$.
For satellites at higher orbiting altitudes, such as GNSS and GEO satellites that feature planar CCR arrays, it is assumed that these always point nadir towards the Earth, i.e. towards Earth's centre. Then, the maximum incidence angle is limited by the geometry of the orbit,

$$\theta_{i,max,(gnss,geo)} = \arcsin\left(\frac{R_E \sin\left(\frac{\pi}{2} + \alpha_e\right)}{R_E + h_{sat}}\right) \tag{2.35}$$

[28], assuming the Earth is spherical. The maximal incidence angle can therefore feature the two possibilities $\theta_{i,max} \in \{\theta_c, \theta_{i,max,(gnss,geo)}\}$.

Deriving the mean optical cross section

A common approach is to determine the mean of the OCS over a set of incidence angles and the velocity aberration annulus, which is described in the following. When the effects of the incidence angle θ_i and the spoiling are taken into account, the FFDP yields

$$\sigma_{eff}(\theta, \theta_i) = \begin{cases} \eta^2(\theta_i)\frac{\sigma(x(\theta_i))}{(2n_\delta)^2} & \text{if } \delta \neq 0 \\ \eta^2(\theta_i)\sigma(x(\theta_i)) & \text{if } \delta = 0. \end{cases} \tag{2.36}$$

The FFDP is averaged for multiple incidence angles θ_i and the range of compensated velocity aberration α_s, which are specified by

$$\theta_i \in [0, \theta_{i,max}]$$
$$\theta \in [\alpha_{s,min}, \alpha_{s,max}]$$

The number of elements in each interval are set to $|\theta_i| = 100$ and $|\theta| = 300$, respectively. These values seem to be appropriate for the calculations, in order to achieve reasonable results. The intervals are used to determine the average optical cross section σ, according to

$$\sigma = \frac{1}{|\theta_i|}\frac{1}{|\theta|}\left(\sum_{\theta_i}\sum_{\theta}\sigma_{eff}(\theta, \theta_i)\right). \tag{2.37}$$

In Figure 2.6, the OCS is plotted over the the off-axis angle θ for different incidence angles θ_i. The presented data originate from a retroreflector with the diameter $D_{ccr} = 38\,\text{mm}$, the wavelength $\lambda = 1064\,\text{nm}$, the single dihedral angle offset $\delta = 3.8''$, and the orbit altitude $h_{sat} = 500\,\text{km}$. The annulus of the velocity aberration for this orbit is in between 24.9 µrad and 50.8 µrad.

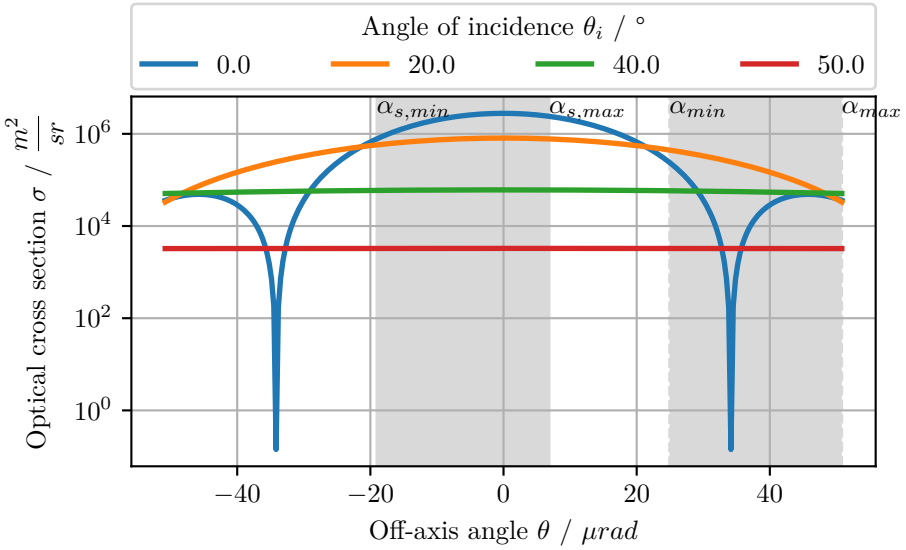

Figure 2.6: OCS $\sigma_{eff}(\theta)$ derived for multiple incidence angles, showing the range of velocity aberration and the shifted annulus. Calculation inputs: $\lambda = 1064\,\text{nm}$, $D_{ccr} = 38\,\text{mm}$, $\lambda = 1064\,\text{nm}$, $\delta = 3.8''$, $\rho = 0.78$, $n = 1.461$, $h_{sat} = 500\,\text{km}$. The areas marked in grey reflect the annulus of the velocity aberration and the compensated velocity aberration due to spoiling.

It can be seen in Figure 2.6 that the annulus of the uncompensated velocity aberration α is located in the region of the minor peaks. The dihedral offset shifts the annulus and consequently the range of the velocity aberration into the area of the main lobe. In consequence, increases the achievable signal strength. Additionally, it can be seen that the peak cross section decreases with increasing incidence angles, up to two orders of magnitude for $\theta_i = 50°$, for this specific case. It has to be noted that this decrease greatly depends on the utilised CCR, but also on the orbit altitude and the wavelength. Accordingly, can not be assumed to be identical for all CCRs. This is a major uncertainty that can't be considered in the link budget, since the orientation of the satellite is unknown and can vary by each overflight. For this reason, the mean OCS is derived from multiple incident angles.
The mean value σ in the displayed case is derived by determining the mean along the incident angles and the grey area, which indicates the aberration annulus from $\alpha_{s,min}$ to $\alpha_{s,max}$.

2.5.3 Spherical satellites

Spherical satellites play a major role in terms of space geodesy. They are heavy, passive satellites that are covered with mirrors and CCRs. The spherical shape significantly re-

duces the spacecraft complexity, including the need for stabilisation and thus power. This enables the realisation of missions that last many decades or even generations [29]. Deriving the OCS of spherical orientated OCSs is more complex as stated up to now. If the reflectors are evenly distributed over the surface, Degnan proposes a simplified approach to obtain the OCS $\sigma_{sphere}(\theta)$ for spherical satellites by

$$\sigma_{eff,sphere}(\theta) = \frac{\sigma(\theta) N_{ccr}}{2} \left[1 - \frac{\sin\left(\frac{\theta_{i,max}}{2}\right)^2}{\left(\frac{\theta_{i,max}}{2}\right)^2} \right]. \tag{2.38}$$

[4]. Equation 2.38 is a function of the off-axis angle θ, the number of CCRs and the maximum incidence angle θ_i. This expression omits the dependency of the incidence angle. As described above, this can be averaged over the velocity aberration annulus, yielding

$$\sigma_{sphere} = \frac{1}{|\theta|} \left(\sum_{\theta} \sigma_{eff,shpere}(\theta) \right). \tag{2.39}$$

3 Data collection

This chapter describes the collection of the SLR measurements. These comprise the publicly available data provided by the ILRS and the data obtained from the DLR system, the miniSLR. In addition, measurements from the former DLR system, the Uhlandshoehe Research Observatory (UROL) are considered [30]. The data for this study originate from the introduced normal points, which contain information regarding the mean detected returns per fired laser pulse. The collected data is summarised in a database for better integrity and handling. All of these points will be discussed in the following.

3.1 Satellite Laser Ranging measurements

As a first step, an overview of the data sources, their storage, and their maintenance is given. The three tasks can be summarised under the term data management, which has the objective to maintain the integrity of the data.
In order to standardise the format of the normal point files, the ILRS has introduced the Consolidated Laser Ranging Data (CRD) format [31]. The stated files contain several sections, which are dedicated to the pass information, the system specifications, and data records. The first is the header section that contains information regarding the target, the station, and the session time. The second is the configuration section that provides the system configuration, e.g., the laser and detector specifications. The last section contains the dynamic data records, e.g., the time series of several normal point records of which each is allocated to an individual time stamp.
Furthermore, the file may contain additional records, such as meteorological data, pointing angles of the system or range and meteorological supplement data. Relevant for the link budget are the pointing angles and the visibility. The latter is available in the meteorological supplement records. For further information, the reader is referred to [31].

3.1.1 Data collection and management

The normal point files from the ILRS stations are publicly available and already processed, whereas the measurements of the DLR systems have to be processed in order to generate the normal points from the ranging data.

DLR systems

Prior and during the time of this thesis, several measurements have been conducted with the miniSLR system. The system is at this stage only able to operate when it is dark, i.e. at night, to prevent saturation of the detector. In the near future it shall be possible to conduct daytime ranging, by implementing a range gate generator, in order to further reduce background noise. Any further necessities for daytime ranging are already fulfilled. Nevertheless, several measurement campaigns have been conducted. The focus of the

conducted measurements was set on the LEO and geodetic satellites, in order to evaluate and validate the systems operation and performance.
However, due to problems with the laser pointing or tracking of the satellite, not all measured passes provide successful data. Tracking is particularly difficult when the satellite is not visible, i.e. cannot be tracked optically. In this case, a successful measurement depends on the given orbit predictions and the user's experience and sensitivity in tuning the laser pointing direction. This means that the pointing of the laser is manually readjusted until a visible signal is received from the satellite. The miniSLR also featured problems with the stability of the laser pointing for some time. This made observations rather difficult, since the laser pointing was quite unstable and had to be readjusted after a period of a few passes. Nevertheless, unsuitable weather conditions, such as local clouds or aircrafts crossing the system's field of view, may hinder measurements. But also the pure range to the target impedes the success of a measurement.
The latter can be exemplary seen in Figure 3.1. Figure 3.1a shows the raw data of Grace-Fo, which is a LEO satellite with an orbit altitude of 500 km. Here, a clear distinction between noise and satellite signature can be made. In Figure 3.1b Etalon-2 has been ranged, which exhibits a orbit altitude of roughly 19,000 km. In this case it is difficult to distinguish the noise from the satellites signature. However, it was able to filter the data, despite the marginal visible satellite track.

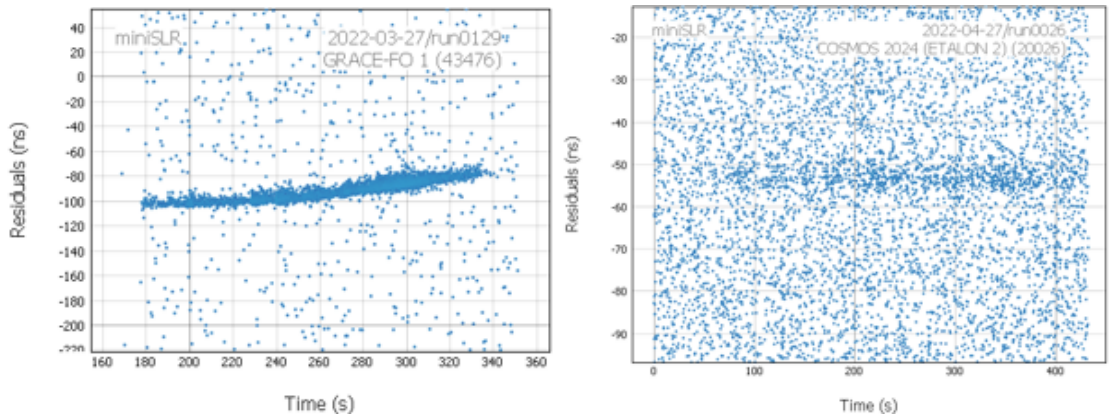

(a) Raw residual ranging data of the LEO satellite Grace-Fo, obtained with the miniSLR at 2022-03-27.

(b) Raw residual ranging data of the GNSS satellite Etalon-2, obtained with the miniSLR at 2022-04-27.

Figure 3.1: In a) a clear track is visible in the ranging data, whereas in b) it is not clearly possible to distinguish the track from the noise.

The overall inspected measurements with the miniSLR were conducted from 2022-03-26 to 2022-08-13.
Processing the data is accomplished as described in Chapter 2.4. OOOS enables the filtering and generation of the dedicated normal points of each observation, which are then written to the individual files in the introduced CRD format. An overview of the successful observations, which enabled the generation of normal points can be seen in Figure 3.2.

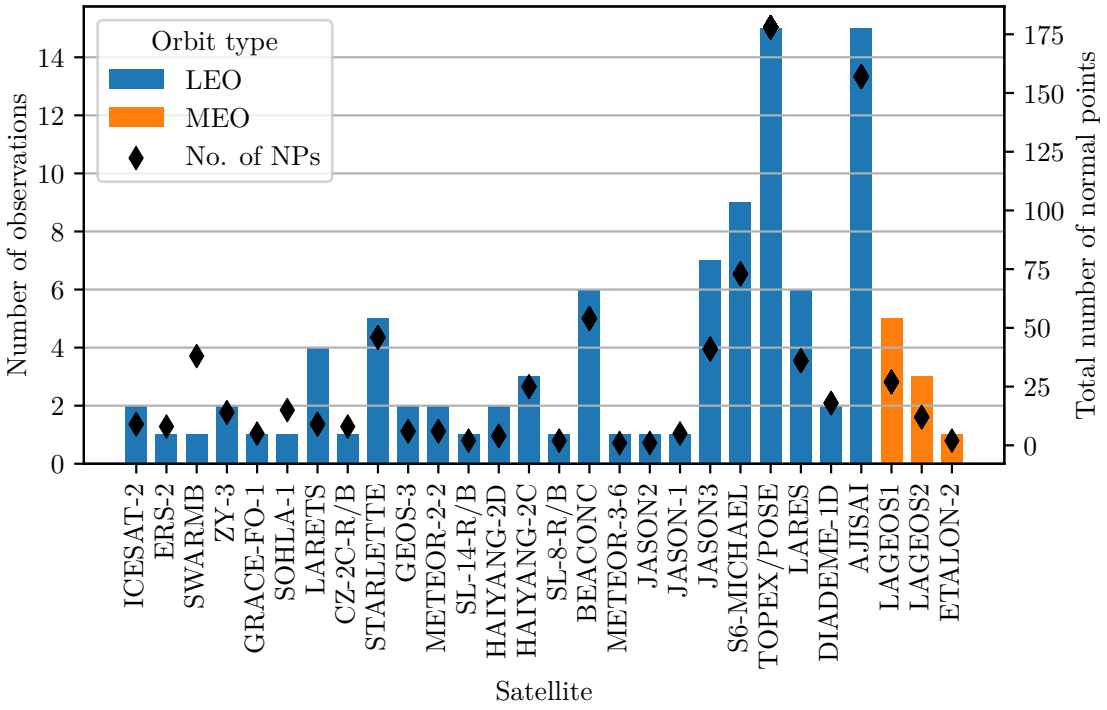

Figure 3.2: Number of successfully conducted observations (left axis) and the total number of normal points (right axis) obtained from measurements with the miniSLR system. The satellites are ordered by their mean orbit height. The measurements were conducted from 26-03-2022 to 13-08-2022.

The observed satellites are differentiated between the orbit types LEO and Mid Earth Orbit (MEO), which are marked in blue and orange colour, respectively. The LEO is declared up to an orbit height of 2000 km, whereas the MEO is declared above 2000 km and up to 35,780 km [32].
Furthermore, the total number of generated normal points is given, which are indicated by the diamonds. In Figure 3.2 it can be seen that a variety of satellites have been ranged, in total 23. Seven of these are spherical, solely exploited for space geodesy. These include Larets, Starlette, Lares, Ajisai, Lageos1, Lageos2 and Etalon2. Cosequently, the miniSLR currently ranged most of the geodetic satellites that are momentarily in orbit.
The satellites Ajisai and Topex peak with a total number of measurements of 15. Ajisai is in addition to the retroreflectors covered with mirrors. This makes optical tracking particularly easy when the satellite is illuminated by the Sun. Topex on the other hand features a large CCR array and thus, makes it easy to range, since a strong returned signal can be expected. The operation of the satellite ended though in the beginning of 2006 [33]. Therefore, orbit predictions are inaccurate and making it difficult to track if no optical tracking can be conducted.
Etalon-2 on the other hand is a spherical satellite that exhibits an orbit height of more than 19,000 km, which is in the range of GNSS satellites. The fact that the miniSLR was able to range this satellite, despite the distance, testifies its performance.

The UROL system on the other hand pursued the concept of a high repetition frequency (up to 100 kHz) SLR. The system successfully operated from 2015 to 2018 [30]. Data

used within this thesis is based on measurements that were carried out from 2018-04-07 to 2018-07-13.
The key specifications of the two DLR system are summarised in Table 3.1.

Table 3.1: Overview of the system specifications of the miniSLR and UROL.

Parameter	miniSLR	UROL
Wavelength	1064 nm	1060 nm
Pulse energy	110 µJ	100 µJ
Pulse duration	4 ns	13 ns
Repetition rate	27 kH	100 kH
Apertures (Rx / Tx)	20 cm / 7 cm	42 cm / 10 cm
Beam divergence	$\approx$ 50 µrad	$\approx$ 250 µrad
Transmitter efficiency	0.7	0.2
Receiver efficiency	0.2	0.5
Pointing/Tracking error	$\approx$ 25 µrad	$\approx$ 240 µrad

Likewise the miniSLR, UROL operated in the Near Infrared (NIR) spectrum of light, but features a much larger beam divergence in comparison. Despite the larger beam divergence, aperture and repetition frequency, both of the system feature similar specifications.
In the process of generating the normal point files for UROL, it has been noticed that in some of the files a pulse energy of 0.002 mJ is present. After checking the data sheet of the laser [34], this pulse energy with the dedicated pulse duration is not present. This probably occurs due to a software issue with OOOS, since several updates were implemented after the operation of UROL. Presumably, default values were written to the files. Due to this fact, the measurements including this pulse energy are omitted. Furthermore, the system could be operated in burst mode at a repetition rate of 200 kHz. In this case the effective repetition rate is half of the burst mode rate.

ILRS stations

The ILRS network comprises roughly 40 active stations all around the world, whereby most of them are located on the upper hemisphere [3], which can be seen in Figure 3.3.
To date a vast amount of stations are not in operation any more, but may provide valuable data. Therefore, these are also included in this thesis and are apparent in the figure below. In total data from 54 stations is obtained that comprises 52 ILRS stations and the miniSLR and UROL, respectively. A list of all stations along with their dedicated code, which is utilised in the course of this work can be found on the ILRS webpage [20] and are summarised in Table A.4 in Appendix A.

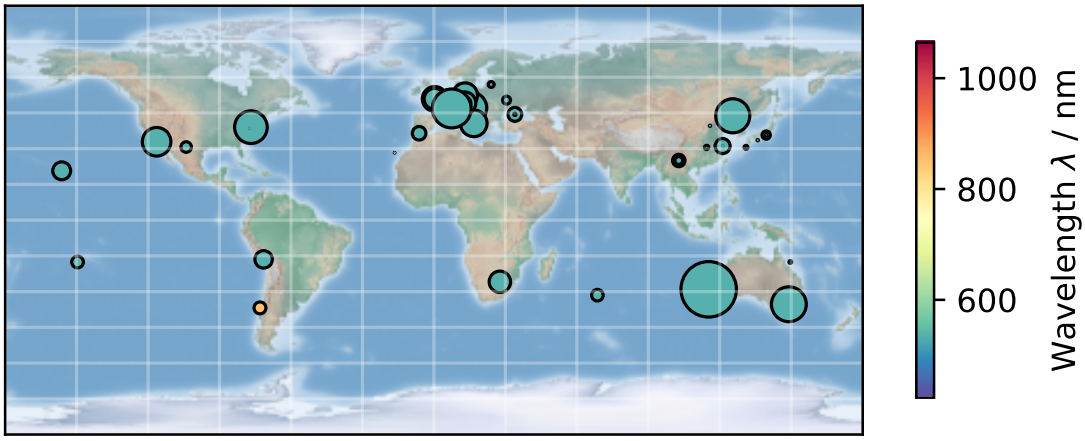

Figure 3.3: Stations of the ILRS around the world for which SLR data is obtained from, distinguished by their ranging wavelength. Further, the size of the dots indicate their contribution to the ILRS in terms of normal points.

The figure anticipates how much data, in term of normal points the stations provide, which is represented by the size of the circles. The stations of the ILRS utilise four different wavelengths. These are 423.5 nm, 532 nm, 849 nm and 1064 nm. Whereby the first was utilised by the inactive station CONL (7405) Concepcion, Chile and the second by the same station and in addition from SOSW (7827) Wettzell, Germany. Since these are barely in use for SLR so far and not of interest for the miniSLR, they are not considered in this work. The most common wavelength is 532 nm, whereas the wavelength of 1064 nm is utilised by six stations that include the two DLR systems. The other stations utilising 1064 nm are IZ1L (7701) in Izaña (Tenerife), Spain, GRSM (7845) in Grasse, France, WETL (8834) in Wettzel, Germany and SHA2 (7821) in Shanghai, China.

The data centres of the ILRS, are the main provider of SLR related data. They archive and distribute the SLR measurements from the contributing ILRS stations. Prior to the distribution of the data, the Operation Center (OC) quality check the incoming data, merges it into daily files, and groups them by each satellite. The merged files are then contributed back to the data centres, making them to the stations and other users accessible.
One of the ILRS data centres is the EUROLAS Data Center (EDC) [35], from where the data for this study was solely obtained from. The EDC maintains the SLR related data on a dedicated server that is publicly accessible [20].
Currently there are two CRD formats, for which normal point data is available on the server. To not miss out any data, both versions are considered while duplicate files and passes are removed.
The data obtained from the EDC dedicated File Transfer Protocol (FTP) server comprises observations from the 07-04-2007 to the 25-08-2022.

Data management

In total more than 300,000 CRD files are obtained from the EDC that contain the data of the 15 year period. In order to manage the collected and generated data from the individual CRD files, the data is maintained in a relational database. The database itself

contains the individual tables, which are assigned to the distinct information and records of the files. Each observation is assigned to an unique observation ID, linking the relation of the individual tables.
The structure of the database can be seen in Figure 3.4.

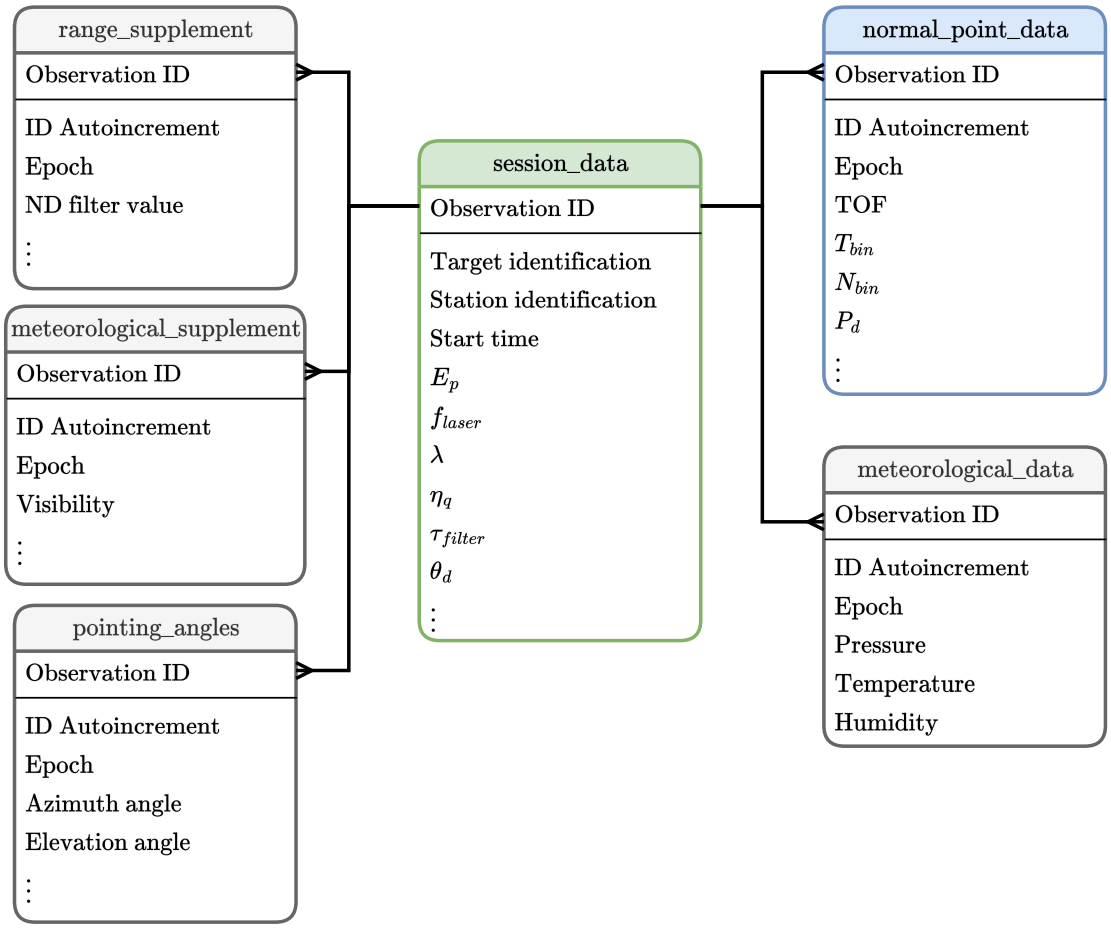

Figure 3.4: Structure of the relational database, which manages the CRD data in dedicated tables. An unique observation ID relates a one-to-many relationship between the tables.

Due to the varying number of dynamical records, each record type is dedicated to an individual table. The main `session_data` table contains the unique session information, e.g., the station, the target and the time of observation. Furthermore, it is dedicated to the applied system specifications during the observation. The remaining tables are dedicated to the individual dynamical records, such as the normal points, which are individually denoted by a time stamp, i.e, epoch. Further supplement data comprises range, meteorological and pointing angles.
The main advantage of using a relational database is the easy access, extraction and combining of the data from the individual tables. The database can easily be expanded to append additional observations, which is conducted by incriminating the observation ID. Due to the one-to-many relationship only the data in the `session_data` table has to be manipulated or deleted, automatically cascading this operation to the other tables. The

auto incremented ID in the child tables allows checking for duplicate records, since the combination of observation ID and auto incremented ID has to be unique.

Nevertheless, not all of the necessary parameters for the link budget evaluation are provided by the CRD files. To complete the data further files become necessary, namely the station log files, which are also available on the EDC server. The individual ILRS station maintains a log file that contains information regarding the station's geographic position, the hardware specifications, and the operating status. Any hardware upgrades or changes are logged in these files along with the date of installation or change, respectively. The relevant data (see Table 3.2) is extracted from the individual log files and written to a single file to enable a better handling.

Table 3.2: Station specifications obtained from the station log files from the EUROLAS Data Center (EDC) [35].

Parameter	Symbol
Receiving telescope aperture	D_r
Total transmission efficiency receiver path	τ_r
Total transmission efficiency transmitter path	τ_t
Static pointing accuracy	$\Delta\theta_p$
Station altitude above sea level	$h_{station}$
Station latitude	lat
Station longitude	lon

The latter two are not directly related to the link budget calculations, but are necessary for the orbit propagation and determination of the observing angles, which is discussed in Chapter 4.2.

Data issues

However, not all of the data can be utilised for the evaluation, since information regarding the stations specifications is missing. These and further issues are discussed in the following.
In the course of this work it showed that not all of the system parameters, which are relevant for the link budget are available for each individual station. Information may be missing either in the CRD files or in the log files. E.g., the pulse energy, repetition rate, detector efficiency, telescope aperture and further more. 17 out of the total 54 stations exhibit missing information on the system specifications, which can be seen in Figure 3.5.

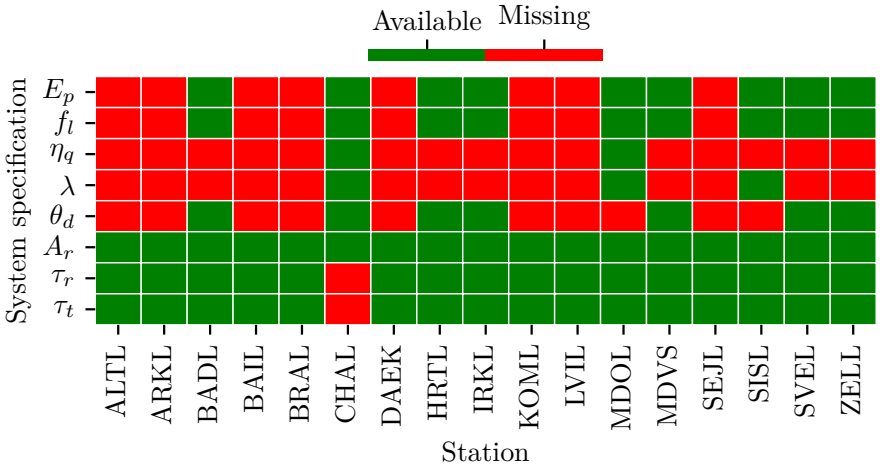

Figure 3.5: Stations with missing specifications for the evaluation of the link budget. Green boxes mark that the information is available and red indicate missing information, respectively. The specifications either stem from the CRD files or the log files.

It shows that for most of the stations, the laser or detector specifications are not declared. These are specified in the CRD files, wheres for station CHAL the transmission efficiencies of the optics τ_r and τ_t are missing, which are specified in the log files. Consequently, 38 stations provide all the necessary information with respect to the ground segment to apply the link budget from Chapter 2.3.

Furthermore, it has been noticed that the return rate P_d that is written into the CRD files can differ to the return rate calculated via Equation 2.15. The cause of this discrepancy is not clear, but can be induced by software issues. The station POT3 (7841) in Potsdam, Germany for example declares much higher return rates as returns in each normal point bin. After clarification with the station operators, this is caused by the software, writing wrong values into the files. Since the origin of this discrepancy is not traceable, the return rate $P_d(N_{pe})$ is calculated via Equation 2.15 and the corresponding photoelectrons per pulse N_{pe} via Equation 2.14.
Besides the return rates, the elevation angle and the atmospheric visibility (see Chapter 2.3) are relevant for the link budget. These measures are input to the atmospheric calculations of the link budget. However, the collected data show that no values for the visibility and only partial values for the elevation angles are present. In order to still be able to infer the elevation angles, a method is proposed in the next chapter.

As a conclusion of this section, some striking anomalies in the data are outlined, which should be considered in future works. It should be mentioned that the data can be very inconsistent, in terms of the units specified in the CRD files, despite the standardisation of the format. But also the data on unknown values can infer the evaluation. Stations can handle Not a Number (NaN) values in a different manner. Another point worth mentioning is the handling of observations that are conducted over midnight. Any midnight transition can lead to shifts of the epochs, but also of the stated start time of observation. The start time serves as the baseline for the individual epochs of the normal points. This can be crucial if any propagation needs to be conducted or the exact epochs are necessary. The

stations should in future provide as much data as possible in the available files, in order to conduct any kind of analysis, e.g., the pointing angles of the system or any signal power attenuation during observation. These are barely or not declared at all.

3.2 Theoretical optical cross sections

Prior to the evaluation of the link budget, the theoretical derivations of some commonly utilised CCR arrays are discussed. These are computed by the method described in Chapter 2.5.
As stated, the method is a simplification of the derivations of Arnold [5] that is proposed by Degnan [6]. The obtained values are utilised to gain a first estimate for reflectors and if the theory is applicable onto the real world SLR measurements. Further, this shall serve as a first estimate of the OCS for the wavelength of 1064 nm, for which no literature values are available. The calculations are conducted for some array types and satellites stated in [36], but also for other satellites calculations are performed.
The calculations require the specifications of the reflectors that are stated in Chapter 2.5. These can mainly be found on the webpage of the ILRS [20]. If not, the webpage often refers to technical notes that are provided by the manufacturer or satellite operators.

3.2.1 Computation

In order to compute the theoretical values, the following specifications need to be known: The CCR diameter D_{ccr}, the depth L_{ccr}, the refractive index n, the reflectivity ρ, the dihedral angle offset δ, the number of offsets n_δ, and the number N_{ccr} of CCRs, which may contribute to the returned signal. Further input are the satellite altitude h_{sat}, the type of the array, i.e., if the satellite is spherical or not, and if the maximum incidence angle is calculated from the orbit geometric or the cut-off angle of the reflector. If the satellite is spherical the OCS is calculated as shown in Equation 2.38.
The reflectivity ρ is barely given in any of the documents or the webpage. Degnan suggests a reflectivity of 0.78 for aluminium coated quartz CCRs and a value of 0.93 for uncoated TIR quartz CCRs [6]. These values are utilised if no reflectivity is available for the CCR. Further, it is assumed that the reflectivity is fairly constant over the wavelength band. Likewise, the value of the refractive index n is often not available for the wavelength of 1064 nm. In this case, the value of 1.45 [37] is utilised, which is valid for quartz CCRs.
The given inputs and the resulting mean OCS σ is written to a dedicated file. Calculations are conducted for the wavelengths λ of 532 nm and 1064 nm.

3.2.2 Evaluating the method

The derived OCS values from the stated method in Chapter 2.5 are evaluated against literature values from [36]. The related literature and self computed values are listed in Table 3.3. The input for the calculation of the theoretical values is listed in Table A.1 in Appendix A. To make the values comparable, the identical orbit altitude is utilised for which the literature values have been computed, which may differ to some extent to the current altitude.

Table 3.3: Literature OCS values derived by Arnold [36, 5] and computed values derived by the method described in Chapter 2.5 for several satellites. *For Ajisai no computations could be performed, due to the lack of CCR specifications.

	OCS / $10^6\,m^2\,sr^{-1}$ (532 nm / 1064 nm)		
Satellite	Literature [5]	Theoretical	CCR array / No.
Lageos	15 / -	3.25 / 1.24	Sphere / 422
Starlette	1.8 / -	1.06 / 0.35	Sphere / 60
Etalon	55 / -	95.4 / 23.7	Sphere / 2140
Champ	1 / -	1.90 / 0.652	Pyramid / 4
Glonass-M	80 / -	81.6 / 20.6	Planar / 112
Ajisai	23* / -	- / -	Sphere / 1436
Galileo-1	-/ -	10.4 / 3.14	Planar / 86
Galileo -2	- / -	4.26 / 1.22	Planar / 60
SwarmB	- / -	1.90 / 0.652	Pyramid / 4
Technosat	- / -	0.028 / 0.012	Single / 14

The calculations are conducted for several types of arrays, which comprise spherical, hemispherical, i.e. pyramid and planar arrays. Taking look at the spherical arrays, i.e., geodetic satellites, such as Lageos, Starlette and Etalon shows that the theoretical values can deviate by a factor of almost five, which is present for Lageos. Starlette and Etalon show discrepancies by a factor of two in both directions.
Champ exhibits a discrepancy of a factor of two above the literature value. This is a pleasing result, since the utilised CCRs only features one dihedral angle offset, whereas the others feature three. The outcome of the calculations for only one offset angle was not clear, since the number of offset angles can vary the OCS by a factor of 36 and further has great influence on the FFDP.
The Glonass-M array is in comparison to the above mentioned ones a planar array, consisting of 121 CCRs. Same as for Champ, the utilised CCRs feature one angle offset. The resulting OCS is despite the assumptions made in Chapter 2.5, surprisingly close to the literature value with an deviation of 2 %. Therefore, planar arrays yield the most accurate results to now.
Another interesting target is Ajisai, which is listed in the table. Apparently, no CCR specifications were found for it and therefore no computations could be performed. It is included, however, because Ajisai is a valuable target for space geodesy.
The comparison of the individual satellites shows that the theoretical calculations reflect the literature values in a reasonable manner, despite the assumptions and errors that can occur. For planar and single reflectors the deviations vary by a factor of two, whereas for spherical arrays these deviations can increase to a factor of five. For a definite assertion more satellites need to be investigated, which is not part of this thesis. Moreover, a more accurate computation could decrease the discrepancies, but therefore more CCR specifications need to be known, which are barely publicly available. These values seem reasonable though for a first estimate. Furthermore, no OCS is available for the wavelength of 1064 nm, therefore no statement can be made. It can be assumed though that the values for the wavelength of 1064 nm are within the same reasonable range as for 532 nm and tend to be a factor of three to four below the ones of 532 nm.

These results are exploited to determine the theoretical OCS of several more satellites, which are listed at the bottom of Table 3.3. These comprise the Galileo constellations, SwarmB and Technosat. The Galileo constellations feature planar arrays with 84 and 60 CCRs [38], respectively. It should be assumed that Galileo exhibits a similar OCS to Glonass-M, since they feature similar orbit altitudes. Galileo first generation has less CCRs, but features larger diameters in comparison to Glonass-M and therefore should yield a similar value. It can be seen that a rather low value of $10 \times 10^6\,\mathrm{m^2\,sr^{-1}}$ results from the computation, which is a factor of eight below Glonass-M.
A decisive statement cannot be made to this finding, but most likely occurs from the smaller dihedral angle offsets in combination of the natural beam split of the uncoated CCRs. The Galileo satellites feature CCRs with three offset angles of $0.8''$, wheres Glonass-M CCRs exhibit a single offset of $2.4''$. Both of the array types comprise uncoated TIR reflectors. Along with the the natural beam split and the small dihedral offset angle, the stated model yields low values. This outcome cannot be extensive validated though, since no literature values are available for the Galileo satellites.

SwarmB features the same array as Champ, but remains on a slightly lower orbit as Champ used to. Nevertheless, the approach yields the same value. Notice that the values differ by almost a factor of two to the theoretical values. Despite the assumptions, this seems reasonable though.
Technosat on the other hand is a interesting target, since it makes use of commercial CCRs of a relatively small diameter of 10 mm [39]. The reflectors are unevenly distributed among the sides of the satellites, wherefore it is assumed that only one CCR contributes to the returned laser beam in general. Taking the small diameter into account yields a relatively small OCS, which is almost two orders of magnitude below the OCS of Champ.

In conclusion it shows that the method stated by Degnan [6] can yield reasonable values for most of the array type, but shows some flaws considering large arrays with uncoated CCRs in combination with small dihedral angle offsets. This can lead to large discrepancies.
Moreover, it is known that the OCS can vary by several orders of magnitude for certain conditions, such as the angle of incidence and the velocity aberration annulus. Both of which can depend on the elevation angle. For a first estimation, however, these averaged values are declared to be sufficient and can be investigated in future studies.

4 Data selection and processing

In the previous chapter, the data collection was explained. This chapter deals with the data selection, i.e., which stations are included in the evaluation. This is a crucial step since Equation 2.14 only applies for single photon returns and not all stations feature a system setup that yields single photon returns in means. Therefore, a filter algorithm is applied, in order to distinguish single photon operating systems from the ones operating at multi photon levels. Moreover, it has also been shown that not all relevant information, such as the elevation angles, are available. For this reason, a method for the determination of these angles is described and evaluated. Then, the data processing algorithm that applies the link budget will be explained.
The previous chapter showed that to date four ranging wavelengths are utilised in SLR. However, only stations that operate at a wavelength of either 532 nm or 1064 nm are considered. The former is the most common wavelength, whereas the latter is of interest for future applications and the miniSLR. The wavelength of 1064 nm offers some technical advantages, such as high power, less atmospheric losses and twice the number of photons per pulse energy in comparison to 532 nm [40]. For these reasons, this wavelength is becoming more and more attractive in SLR and is utilised in the two DLR systems.

4.1 Selecting single photon stations

As stated in Chapter 2.4, single photon operation can be assumed to be present below a return rate of roughly 15 % [17]. To gain first insight of the received signal levels of the individual stations, the return rate distribution of each station is presented in Figure 4.1. The figure shows a boxplot of the return rate of each station, taking all obtained measurements and the operational wavelengths of 532 nm and 1064 nm into account.

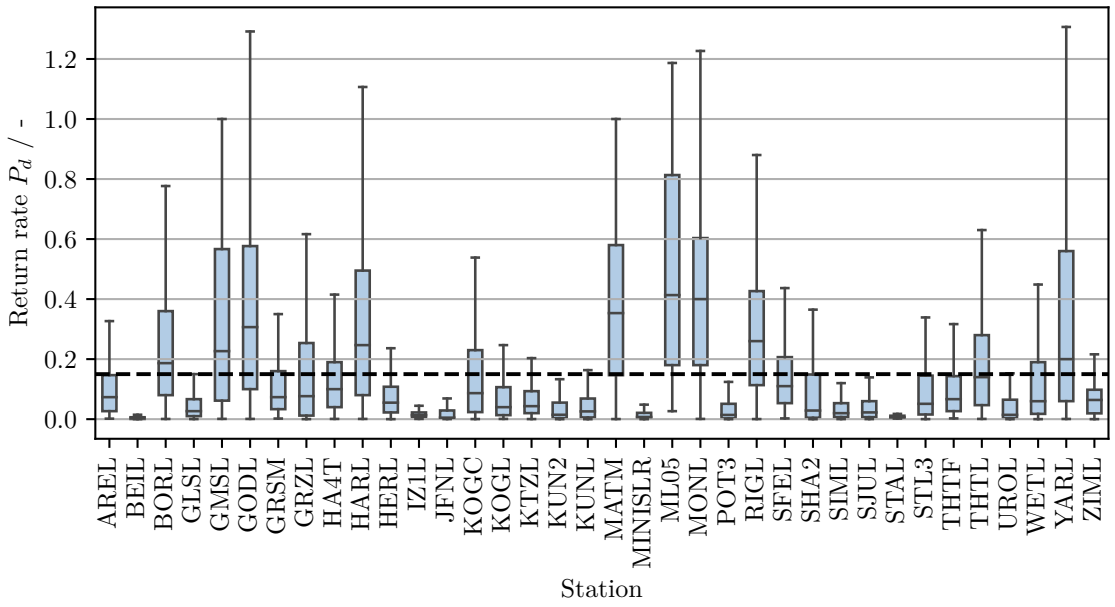

Figure 4.1: Boxplot of the return rate distribution of the individual stations, which takes all the obtained measurements into account. Further the 15 % single photon threshold is displayed.

It can be seen that the return rate can vary from a few percent to 100 % among the stations. It should be noted that a return rate beyond 100 % cannot be achieved and most likely occurs due to software issues, writing a wrong amount of detections per normal point bin into the files. This will not be problematic though, since larger return rates are emitted in the following.
Some stations show distributions solely below 15 % return rate, for which can be assumed that these mainly operate at single photon levels. For other stations this sweeping distinction cannot be made. In this manner a first selection is conducted, employing the single photon threshold, which is displayed in the figure. It is assumed that stations with a median above 15 % mainly operate in multi photon mode and are therefore removed. These include the stations BORL, GMSL, GODL, HARL, MATM, ML05, MONL, RIGL and YARL. Nevertheless, the remaining stations need to be further filtered, to remove any remaining multi photon data sets. These comprise 28 stations.

Another aspect is the ability of stations to perform return rate control and aim to solely operate at single photon levels. This means, the transmitted energy is controlled in a way that the retrieved signal intensity remains in the single photon level, thus below a return rate of roughly 15 %. There are several methods to realise return rate control, which can comprise the insertion of a Neutral Density (ND) filter in the transmitter or receiver path, divergence control, laser energy control, etc. [16]. E.g. station HERL utilises a ND filter and POT3 varies the laser energy.
The return rate control complicates the evaluation of the data, since the attenuation factor of the transmitted signal is not noted in the CRD, nor in the log files and can be highly dynamical. Nevertheless, stations that are capable of this mechanism are considered in the analysis, because it is unknown for which satellites this is applied.
Since it cannot be assured that the remaining stations solely operate at single photon

levels, these are further filtered. Therefore, each station needs to be distinguished by the applied configuration of the hardware, which can yield different return rate distributions. Changes are dedicated to the pulse energy, the pulse width, and the repetition rate of the laser, but further changes can involve the telescope and the detector. However, the returned signal strength is also a function of the distance and the OCS of the reflectors (see Chapter 2.3). Consequently, the return rates of the observed satellites need to be considered in addition.

Therefiore, the stated value of 15 % is exploited as a threshold for the filtering. To account for the altering specifications, the data of each station is grouped by the applied configuration. This includes the laser specifications, such as the wavelength λ, the pulse energy E_p, the laser repetition rate f_l, and the beam divergence θ_d. Additionally, the specifications of the optics, the receiving telescope aperture D_r, the transmission efficiency of the receiver path τ_r, and the transmitter path τ_t are of relevance. Further, the bandpass filter transmission τ_{filter} is included. Lastly, the detector type and the quantum efficiency η_q of the detector is covered. As mentioned, the satellite has influence on the returned signal strength and needs to be considered. Therefore, the data of each configuration is further distinguished by the observed satellites. If the median return rate of the sub-group is below 15 %, the data is declared as single photon, otherwise as multi photon and is removed.
The process of the filter is displayed in Figure 4.2. It groups the data as stated above and decides if the single photon level is fulfilled or not. Wherefore, it removes grouped data sets of a station that exhibits a possible multi photon distribution.

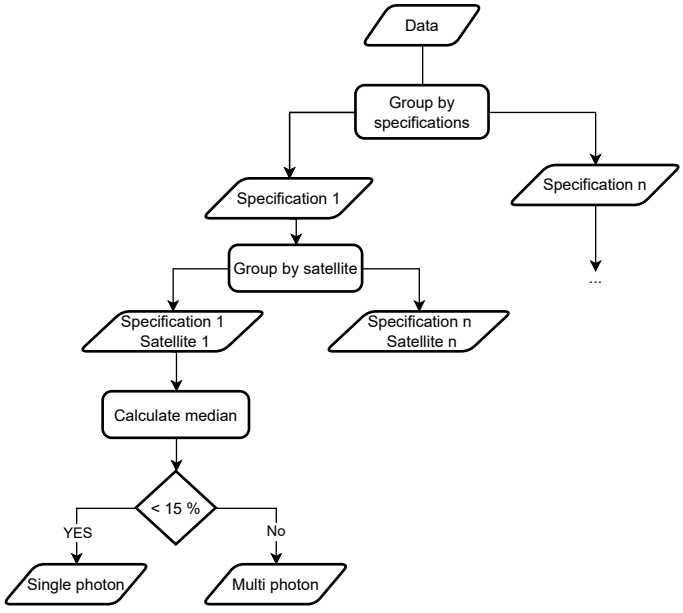

Figure 4.2: Algorithm that groups the data by the applied system specifications and the satellites, in order to receive single photon measurements. The data is declared as single photon when the mean of the return rate is below 15 %.

The remaining stations and their corresponding distribution of the return rates are shown in Figure 4.3.

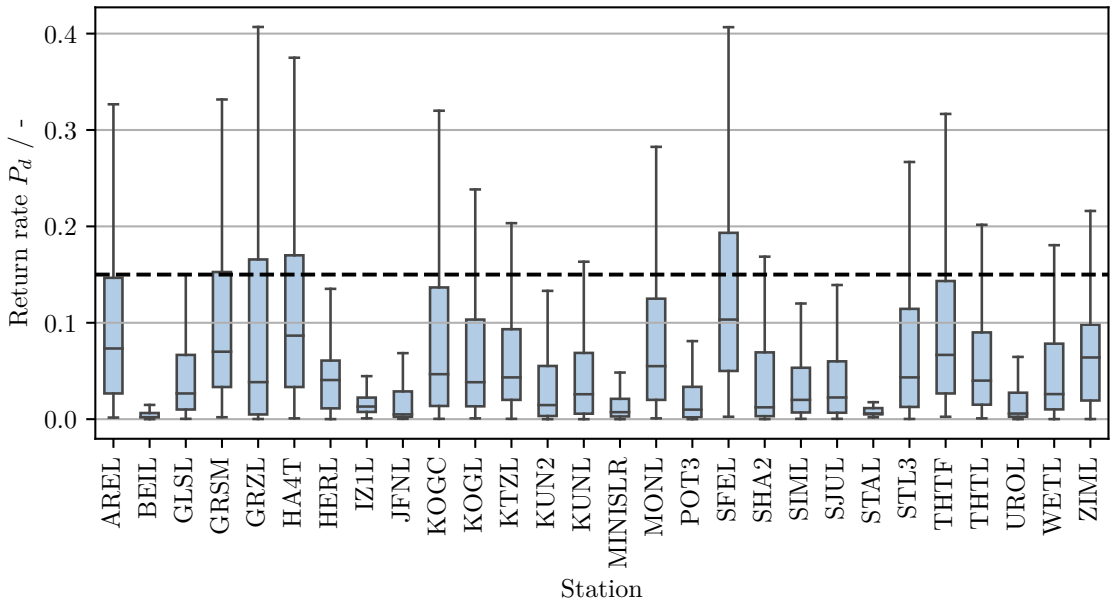

Figure 4.3: Boxplot of the return rate distribution of the remaining stations after post filtering.

It can be seen that the median of the data remains below the 15 % threshold, but the interquartile range may exceed this threshold. This follows from the fact that this method of filtering does not filter every measurement, but a series of measurements, in order to achieve a distribution with a reasonable amount of data points. Filtering the data for the individual measurements would require more input parameters, such as the weather conditions and the tracking error. Both of which can be highly dynamical during a single observation. Consequently, filtering each measurements is not recommended.

4.2 Satellite altitude and observing angles

Turning now to the further missing data, i.e. the elevation angles. In Chapter 2.3 it was shown that the atmospheric transmission is a function of the elevation angles and the station height. The collected data reveals that only partial records are available for the observing angles. In order to retrieve them, the topocentric position of the satellite, which has its origin in the geodetic position of the observer on Earth is determined. Therefore, the satellites position at each normal point epoch needs to be known. This can be achieved by estimating the position by propagating the orbit, i.e. determining the position for a given initial state, taking several perturbations into account. These include the atmospheric drag, the J2 and higher harmonics of Earth's gravitational field, the solar pressure, and the gravitational influence of the Sun and the Moon. A commonly applied orbit propagator is the Simplified General Pertubation (SGP) 4. It accounts for the above-mentioned perturbations and is publicly available [41]. The model inputs are Two Line Elements (TLE) data sets, which contain a snapshot from the orbital elements of a satellite orbiting the Earth. The TLEs sets are provided by *CelesTrak* [42] or *space-track* [41] and are updated on a daily basis. With the TLE and the SGP model, the satellite states, i.e. position and velocity can be estimated for future or past times. The accuracy

of the model decreases gradually with each day, which is why the time difference between the TLE epoch and the propagation time should be kept within a few days. Most likely TLE sets are utilised to estimate the satellites position up to one week.

The outputs of the model are the Cartesian satellite's states in the Earth-Centered-Inertial (ECI) system. Applying an Earth model, such as the common WGS84 model [43] and the consideration of the rotation of Earth in space by the Greenwich sidereal time, enables the determination of the satellites position in an Earth fixed system. Therefore, the determination of the satellites altitude h_{sat} can be conducted. The WGS84 represents the Earth as a rotational ellipsoid under consideration of the flattening of the Earth. Modelling an observer on Earth in the same manner by the geographic coordinates (latitude lat, longitude lon, height above sea level $h_{station}$), enables the determination of the observing angles in a topocentric system. By simple vector operation the topocentric vector is determined and thus, the elevation angle α_e can be retrieved.
A common python library, namely *skyfield* [44], is utilised for the orbit propagation and the derivation of the observation states. The library enables the satellite propagation via the SGP 4 model using the TLE data set. For this reason, historical TLE data is obtained from space-track [41] for the satellites remaining in the data. The calculations for this purpose have been derived and extensively discussed by Kelso available on [42].

In order to validate this method, the obtained angles are compared to the available records from the CRD files. For the evaluation, the records from the station GLSM (7357) in Tanegashima, Japan are considered, since this is the only station that provides consistent records for each normal point. In Figure 4.4 the elevation angle α_e from the declared propagation method is plotted against the elevation angle $\widetilde{\alpha_e}$ recorded by the station.

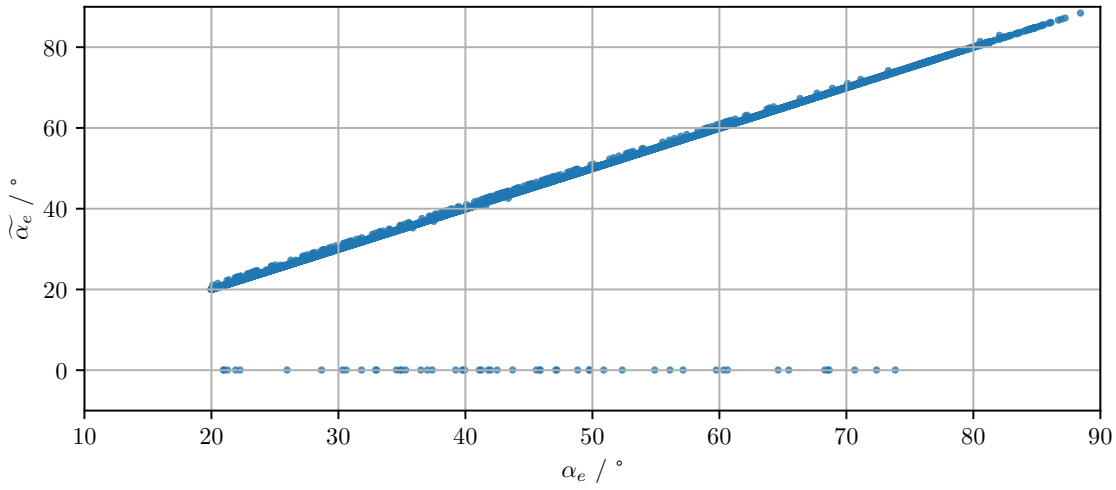

Figure 4.4: Elevation angle α_e from orbit propagation against the elevation angle $\widetilde{\alpha_e}$ recorded in the CRD files from station GLSM (7357).

What strikes out in Figure 4.4 is the strong correlation of the two declared elevation angles. This is underlined by their correlation coefficient of 0.978, Additionally, it can be seen that some of the CRD records do not correlate at all. It turns out that these records contain default values of 0.05°, but only make up 0.045 % of the data. Ignoring the default records results in a correlation coefficient of ≈ 1. This finding confirms that the method described

above yields reasonable values for the elevation angles and is valid for the link budget calculations.

4.3 Processing algorithm

In this section the processing algorithm is explained, which applies the link budget model presented in Chapter 2.3 on the obtained normal point data, along with the declared system specifications.
The only quantity that is still missing is the visibility V, which is relevant for the atmospheric transmission. Since none of the stations record this metric it is assumed with an average visibility of 23.5 km, which corresponds to standard clear atmospheric seeing [15, p. 89].
Now that all quantities are known, the link budget can be applied to the SLR measurements and the OCS can be determined from them. This process is described in Figure 4.5.

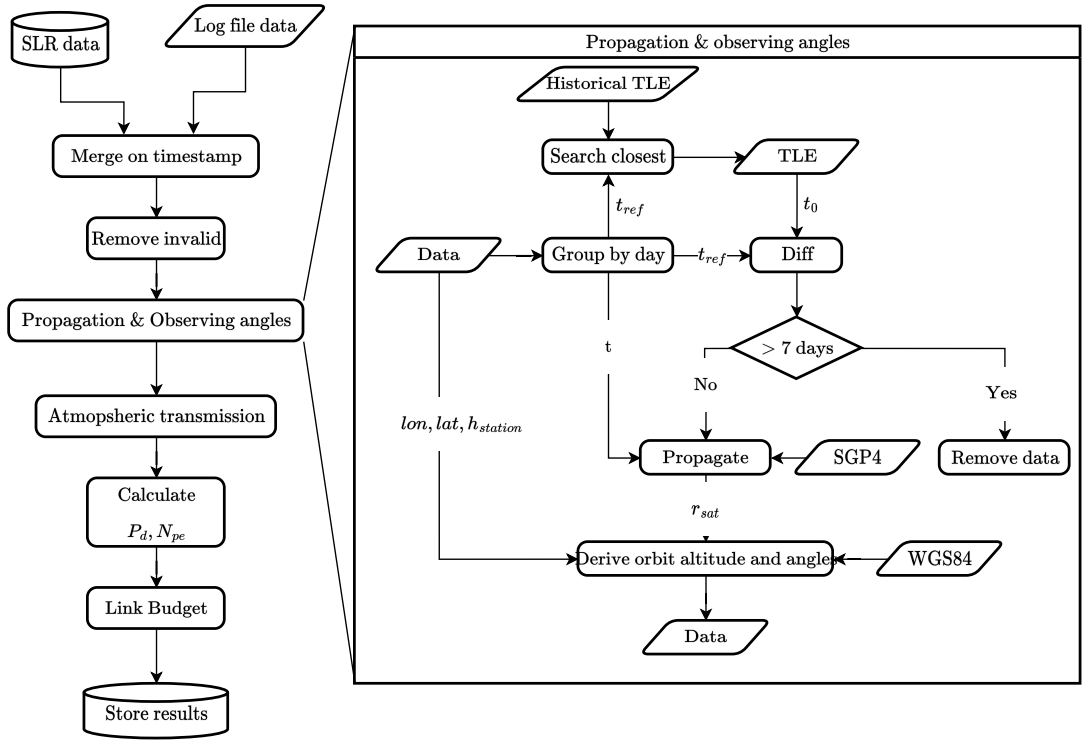

Figure 4.5: Evaluation algorithm to determine the optical cross section, taking the normal point data as input.

The algorithm reads the normal point records along with the available system specifications in the CRD files from the database. To each data point the distinct hardware specifications from the station logging files are appended. In order to match the correct temporal specification, the timestamp of the normal point is compared to the corresponding date of the log.
Any remaining invalid observations in which E_p, f_l, λ, η_q or θ_d have an invalid flag, such as -1 or nan are removed. Due to the fact that SLR station operators frequently change

their hardware settings and it is not clearly traceable which specifications were applied at this moment. This may occur due to partial software issues of the stations.
In the next process the elevation angle α_e of the flyover is determined. Therefore, the data is grouped by each day, taking the first time stamp of the day as reference t_{ref}. For that specific satellite, the closest TLE data set is searched for in the available historical TLE data and the epoch t_0 is extracted from it. If the time difference between the TLE epoch and the reference timestamp $(t_{ref} - t_0)$ is greater than one week, the data of this day is omitted. For the remaining data, the orbit is propagated for each data point, i.e., the epoch t of the normal point, utilising the SGP 4 model. The orbit altitude above sea level h_{sat} and the elevation angle α_e are then determined as described in Chapter 4.2.
The elevation angle α_e, the station altitude above sea level $h_{station}$ and the operating wavelength λ are then input to the next process. It calculates the atmospheric transmission τ_{atm}, as described in Chapter 2.3 for each data point.
The remaining unknown parameters are determined in the next process. The effective telescope area A_r is calculated via Equation 2.6, assuming an obscuration of 25 % for all utilised telescopes. Resulting from the fact that no information on the receiving telescope is available other than the main aperture. The range R to the target is derived from the TOF, as shown in Equation 2.1. The refraction of the atmosphere is in this case neglected, since it only makes up a few meters [4] and the most precise range determination is not of interest. The parameters, such as the number of emitted photons N_t and the transmitter gain G_t are calculated as described in Chapter 2.3. The remaining parameters, the transmission efficiencies of the optics τ_r and τ_t respectively, the filter transmission τ_{filter} and the quantum efficiency η_q are present in the data records.
Next, the return rate is determined via the detected photons in the normal point bin (see Equation 2.15). This metric can then be converted to the actual mean photons per pulse, assuming these are generated under single photon levels (see Equation 2.14). The link budget can then be solved by the OCS for each normal point.
The derived data, along with the given system specifications are then written to a new database file, which ensures easy access and processing of the data.

5 Results

This chapter comprises the findings of the OCS values that are derived from the SLR measurements via the link budget equation (see Chapter 2.3). The main goal is to derive an overall OCS of each satellite, which can be used for signal estimations. Since it cannot be assured that each station yields the same values, the resulting OCS among the stations is evaluated for a selection of satellites in different orbit altitudes. Therefore, a method is proposed to identify stations that yield reasonable and consistent values. The remaining stations are then used to determine the OCS of the remaining satellites in the data.
After the OCS values are derived, they are compared to the partially determined theoretical values, which shall give insight on the derivations of the link budget. Lastly, in Chapter 5.3, the signal estimation for selected satellites is conducted for the miniSLR. This should provide insight about whether the selected targets can be ranged reasonably.

5.1 Evaluating the stations

As a first step, the overall OCS distribution of the single photon stations is investigated. This enables the identification of any major outliers. The OCS distribution of the stations is displayed as a boxplot in Figure 5.1.

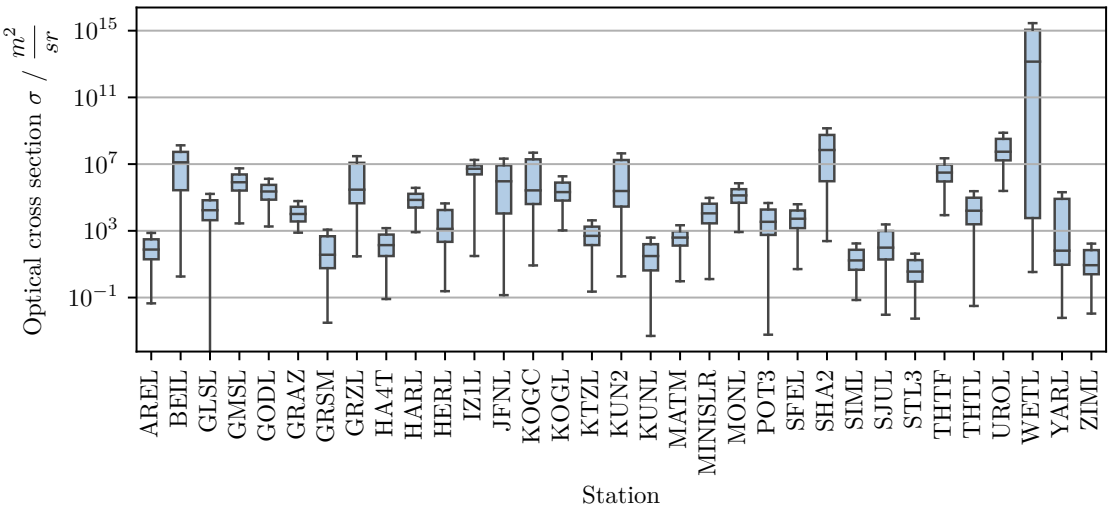

Figure 5.1: Boxplot of the OCS distribution of the individual single photon stations, derived from the link budget.

What strikes out in the figure is that station WETL exposes much higher OCSs than the other stations. The median of all other stations ranges between $10\,\mathrm{m^2\,sr^{-1}}$ and $10^6\,\mathrm{m^2\,sr^{-1}}$, whereas station WETL features a median of about $10^{13}\,\mathrm{m^2\,sr^{-1}}$. The data reveals that this station partially declares a beam divergence of $1''$. In contrast, the beam pointing error,

which is utilised for the link budget and is taken from the log file, states 2″. Consequently, Equation 2.4 results in a very low transmitter gain, since the pointing loss assumes a value of almost 100 %. Conversely, large values result for the OCS. Due to this finding, the data for station WETL with the beam divergence of 1″ is not taken into account in the following sections. This makes up roughly 35 % of the data from this station.
Figure 5.1 additionally reveals OCS values close to zero in the individual distributions. These are probably caused by several normal points featuring return rates close to zero and thus yielding low OCSs. These low return rates may occur due to larger pointing or tracking uncertainties, but also local clouds or rain could interfere with the returned signal.
It can be further seen that several stations yield low OCSs while others exhibit much greater values. This can be a first indicator of the ranged targets of the station. LEO satellites exhibit due to their lower altitude compared to MEO or GEO satellites, a lesser amount of CCRs and consequently a lower OCS. Therefore, lower distributions can indicate that a station mainly ranges LEO satellites and greater distributions indicate ranging of MEO satellites and above.

In the following, a selection of targets is investigated, which shall enable the distinction of stations that yield reasonable and consistent values for the OCS. For this reason, the derived median of each station is considered. In Figure 5.1 it has been revealed that stations can yield values close to zero. These, but also larger outliers, can bias the mean in either direction. Therefore, only the median is taken into account, since tt is not as susceptible to outliers as the mean. The remaining errors and variations are visualised by the lower 25 % and upper 75 % quantiles, which are displayed as black error caps in the figures.
The resulting OCSs of the stations is distinguished by the two wavelengths of 532 nm and 1064 nm, since the resulting OCS is in theory greatly dependent on the utilised wavelength (see Chapter 2.5).

5.1.1 Lageos satellites

A first measure for the evaluation is to investigate the findings of geodetic satellites. Promising targets are the spherical Lageos satellites, which are in orbit for more than three decades and are exploited for space geodesy [20]. Moreover, these are used to characterise the precision of a system and therefore are ranged by most of the stations. The Lageos satellites orbit on a MEO around Earth, with an altitude of roughly 5800 km. In Figure 5.2 the median OCSs of the individual stations for Lageos-1, which are derived from the link budget, are visualised.

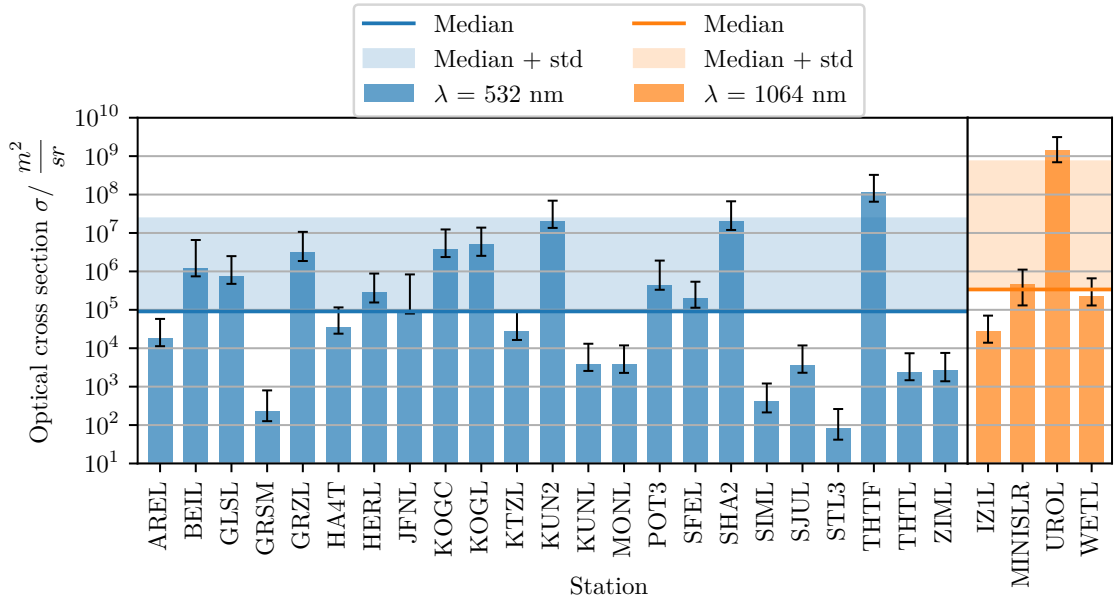

Figure 5.2: Median OCS of Lageos-1, derived from the link budget of the individual stations. Furthermore, one standard deviation to the median of the displayed values is shown. The black error caps display the lower 25 % and upper 75 % quantile of the data. The data comprises measurements from 2008-10-29 to 2022-08-13

What stands out in the figure are the great variances of several orders of magnitude among both wavelengths. Additionally, the displayed error caps reveal that the distribution of the data can vary by up to one order of magnitude. These large variations in the measurements, can be attributed to varying weather conditions or pointing uncertainties. These metrics have a significant effect on the signal strength and therefore on the outcome of the link budget.
In order to enable a qualitative comparison among the stations, the median resulting from the displayed values is shown. For the wavelength of 532 nm it can be seen that multiple stations feature values that are several orders of magnitude below the resulting median. These large discrepancies can most likely be attributed to incorrect stated system specifications, such as the beam divergence or the pointing error.
Furthermore, several stations show values that are less than one order of magnitude below the median. Most likely resulting from applied return rate control or also incorrect stated system specifications, but to a lesser extent.
Since multiple stations feature relatively low values, which shifts the median to a lower value, the median can be introduced as a lower limit. On the other hand, some stations feature values that are several orders of magnitude above the median. These values most likely originate from an overestimation of the system losses, which can especially be seen for UROL. Hence, the stated system losses for these stations may be less in reality. For this reason, an upper limit of one standard deviation to the median is introduced. Consequently, the resulting range of the median and upper limit shall enable the differentiation between stations that either perform return rate control, state incorrect system specifications or feature larger tracking or pointing uncertainties. It hast to be mentioned though that

these limits are not absolute and thus only serve as an indicator to qualitative evaluate the outcomes of the individual stations.
The utilised link budget model does not consider all the occurring losses, nor any dynamical behaviour of the stations and environmental impacts, due to the lack of information. Therefore, a more precise model, along with further declared specifications could yield different OCSs, shifting them in either direction. Nevertheless, it is assumed that the stations that yield values above or close to the upper limit most likely represent system losses that are lower in reality. For stations that yield values below or close to the the lower limit it is assumed that these either perform return rate control, underestimate their system losses or exhibit larger tracking uncertainties in reality.

Considering the various uncertainties, the stations BEIL, GLSL, GRZL, HERL, KOGC and KOGL may yield reasonable values for the wavelength of 532 nm. The stations that show values close or below the median either underestimate their losses or perform return rate control. Some in a greater extent than others, such as GRMS, SIML and STL3 that feature noticeable low values below $10^3\,\mathrm{m^2\,sr^{-1}}$. On the other side, the stations KUN2, SHA2 and THTF exhibit values close to or above the resulting upper limit and thus most likely overestimate their system losses. The evaluation is more difficult for the wavelength of 1064 nm, because only a small number of stations utilises this wavelength, which results in an unclear outcome. This is why the median and upper limit should be taken with caution, and a comparison among both wavelengths should be taken into account. This is reasonable, because the discrepancies among the stations, are much greater than the expected variance of the two wavelengths. What stands out in the Figure 5.2 is that UROL features a mean value that is more than three orders of magnitude above the median. Therefore, most likely overestimates the system losses. Station IZ1L either performs return rate control or underestimates the system losses, but remains one order of magnitude below the miniSLR.
Lageos-2 reveals similar patterns and is therefore not included here. The outcome of Lageos-2 can be found in Figure A.1 in Appendix A.

5.1.2 Etalon and GNSS satellites

From the findings so far it is not fully clear if the stations that exhibit values close or below the median, perform either return rate control or feature larger losses than stated. This follows from the fact that Lageos may return a strong signal, due to the large amount of CCRs and the rather low MEO altitude. Therefore, satellites at higher altitudes are investigated. Since the miniSLR was previously able to range Etalon-2, which features an orbit altitude of 19,000 km, this satellite is observed. In fact, Etalon-1 and Etalon-2 are designed identical and remain on similar orbits, wherefore the measurements of both satellites are summarised.
Due to their large orbit altitudes, it is assumed that for the Etalon and GNSS satellites no return rate control is performed. This follows from the fact that the returned signal is a function of the slant range inverse to the power of four (see Equation 2.2). Consequently, by an increase of the orbit altitude of a factor of three, the returned signal strength should decrease by the factor of 81.
The combined derived OCSs of Etalon-1 and Etalon-2 are shown in Figure 5.3.

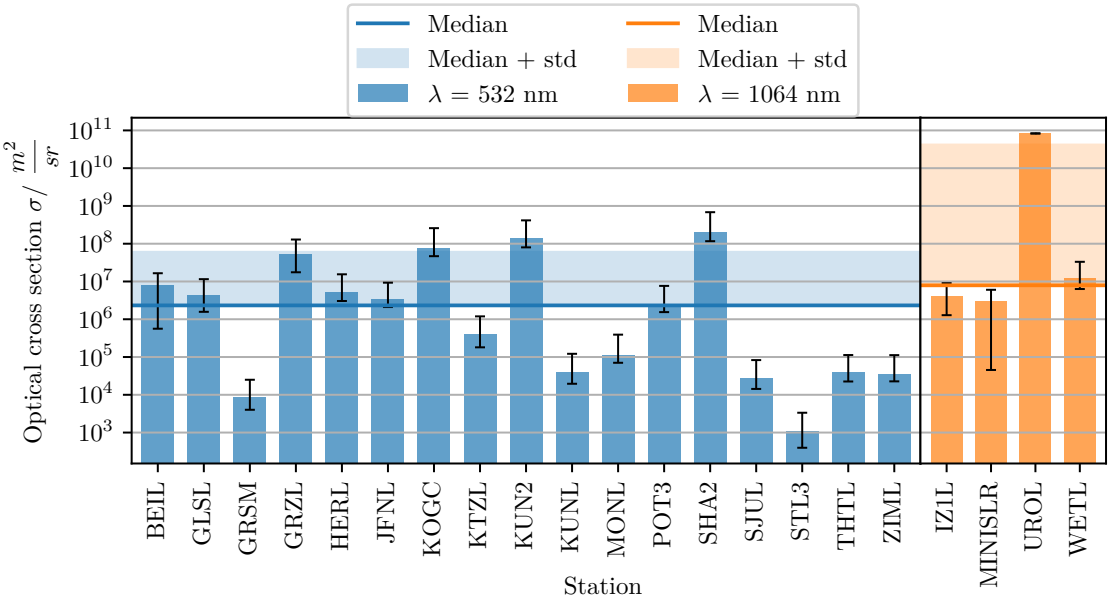

Figure 5.3: Median OCS of the combined data of Etalon-1 and Etalon-2, derived from the link budget of the individual stations. The satellites are designed identically and maintain on an orbit altitude of 19,100 km. The data comprises measurements from 2008-11-13 to 2022-08-07

It can be seen that the miniSLR features a large variance. This results from the fact that only two normal points contribute to the OCS. In spite of the fewer amount of data points, the OCS seems reasonable. Assuming the resulting range of the median and standard deviation is reasonable, reveals that the stations BEIL, GLSL, GRZL, HERL, JFNL and POT3 yield plausible values for the wavelength of 532 nm.
For the wavelength of 1064 nm it can clearly be seen that UROL exhibits as previously an implausible large value, whereas IZ1L, miniSLR and WETL yield reasonable ones.
These findings are confirmed by the GNSS constellations Glonass-M and Galileo. Hereby, satellites that feature the same CCR array and similar orbit altitudes are summarised. The figures of the Glonass-M (Figure A.2) and Galileo constellations (Figure A.3, Figure A.4) can be found in the Appendix A. What is evident in the figures, is that SHA2 features values for 1064 nm. But as for 532 nm, these are above the limit and therefore declared as invalid.

To conclude the findings on the Etalon and GNSS satellites, it can be stated that the stations BEIL, GLSL, GRZL, HERL, JFNL and POT3 yield reasonable values for the wavelength of 532 nm. However, the stations GRMS, HARL, KTZL, KUNL, MONL, SIML, SJUL, STL3, THTL and ZIML exhibit values below or close to the resulting median and thus most likely underestimate their losses. In particular the station GRMS, SJUL, STL3, THTL and ZIML exhibit noticeable low OCS values, which are up to three orders of magnitude below plausible values. Furthermore, the stations KOGC, KUN2 and SHA2 exhibit values close to or above the upper limit of one standard deviation to the median. This indicates that these most likely overestimate their system losses.
For the wavelength of 1064 nm the stations IZ1L, WETL and miniSLR exhibit reasonable values, whereas station UROL exhibits values, which are three orders of magnitude above

the median. As seen in Table 3.1, the assumed pointing error is almost as large as the beam divergence. Therefore, the available system specifications do not reflect the reality and are consequently lesser in reality. SHA2 also yields relatively large values, but to a lesser extent than UROL. Nevertheless, this station is also declared as invalid, since it shows noticeable large OCS values for the wavelength of 532 nm.
For the stations AREL, KOGL, SFEL and THTF no single photon data is present for any GNSS satellites and therefore no statement can be made for these stations. Considering the Lageos satellites, it shows that THTF features values that are four orders of magnitude above the median. This result indicates that the station overestimates the losses. AREL and SFEL show to some extent low values in the case of the Lageos satellites. Station KOGL yields reasonable values in the case of Lageos, but could not be evaluated for the Etalon nor GNSS satellites, since no data is available. Nevertheless, it will be considered in the following.

5.1.3 LEO satellites

Turning now to LEO satellites shall reveal which of the selected stations perform return rate control. Another aspect that may influence this outcome are larger tracking uncertainties of LEO satellites, since they feature large relative velocities near zenith. As previously mentioned, the utilised link budget model assumes a constant pointing error, which may also include common tracking uncertainties, but does not consider variations of the tracking error. The following evaluation shall expose which measurements of single photon stations can be utilised for further derivations of the OCSs. A first selection is already achieved by investigating Etalon, GNSS and the Lageos satellites. Therefore, the stations included in the further evaluation are BEIL, GLSL, GRZL, HERL, JFNL, KOGL, POT3, IZ1L, miniSLR and WETL.

The focus is on the satellites that were also ranged with the miniSLR, in order to evaluate the stations utilising the wavelength of 1064 nm. It already has been seen that the miniSLR and WETL yield similar values. Further, it is known that the returned signal strength of LEO satellites is much greater than the ones for Lageos and Etalon. Therefore, it may be assumed that many measurements have been eliminated by filtering for single photon data. To give insight, whether any large outliers are the result of a low amount of data points or other effects, the number of normal points is additionally displayed, which is marked by black diamonds.
Chapter 3.1.1 has revealed for which satellites a reasonable amount of normal points has been obtained with the miniSLR. Therefore, a selection of these satellites is investigated in the following. These comprise satellites that are most likely to be ranged by most of the stations and thus include Ajisai, Starlette, BeaconC and Swarm.

The satellite Ajisai has an orbit altitude of roughly 1500 km, is of spherical shape and likewise Lageos, exploited for space geodesy. The OCSs resulting from the measurements of the stations can be seen in Figure 5.4.

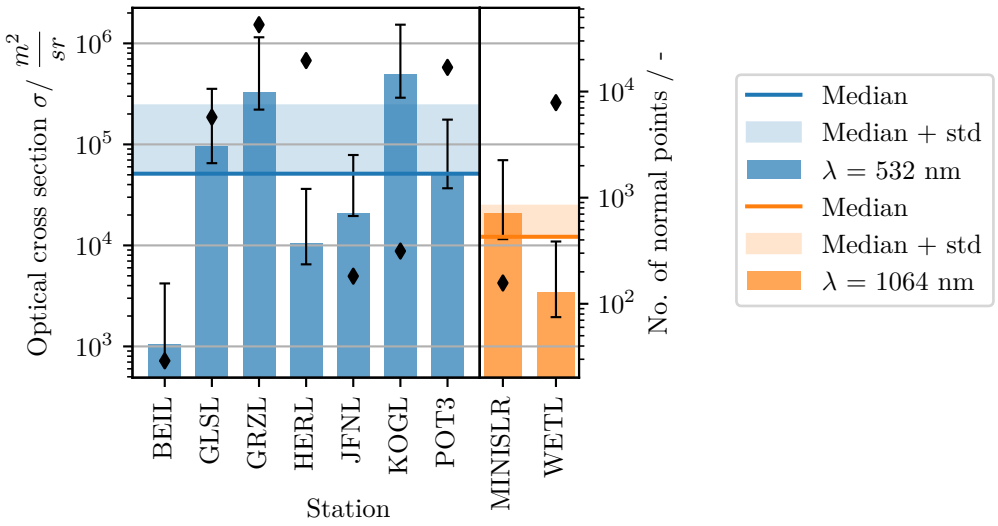

Figure 5.4: Median OCS (left axis) of Ajisai, derived from the link budget of the individual stations. The obtained normal points are displayed as diamonds (right axis). The data comprises measurements from 2009-06-16 to 2022-08-12.

In Figure 5.4 it stands out that station BEIL, which seemed to yield consistent values until now, shows a relatively low OCS. This can most likely be attributed to the low amount of normal points. The data comprises three observations on two consecutive days. One possible explanation could be that unsuitable weather conditions prevailed during these days, thus yielding low OCSs.
Considering the variances that previously appeared among the stations shows that the stations GLSL, GRZL, KOGL and POT3 most likely yield reasonable values. From the station log files it is clear that the stations BEIL, GLSL, JFNL and KOGL do not perform any return rate control. This leads to the fact that JFNL might feature larger tracking errors. In contrast stations HERL and WETL most likely perform return rate control, due to their larger discrepancies towards lower values.

Next, BeaconC is investigated. It is a satellite that is fully covered with CCR panels. In total, the satellite possesses nine panels, each comprising 40 CCR [20]. BeaconC has an orbit altitude of roughly 930 km. Apparently, this is the only LEO satellite, that has been ranged from both stations, the miniSLR and IZ1L in the period of this thesis. Therefore, it is included into the evaluation, to conclude the outcome of station IZ1L.

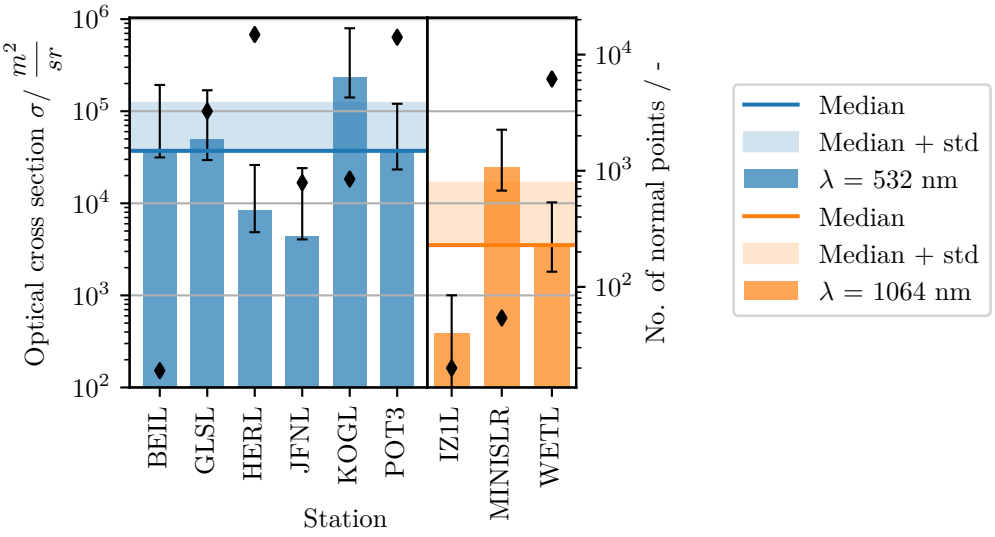

Figure 5.5: Median OCS of BeaconC, derived from the link budget for of the individual stations. The obtained normal points are displayed as diamonds (right axis). The data comprises measurements from 2009-01-17 to 2022-05-25.

Figure 5.5 reveals that the stations BEIL, GLSL, KOGL and POT3 can yield reasonable values. The values for the wavelength of 1064 nm show that the miniSLR is the only station that yields reasonable values, whereas IZ1L and WETL most likely perform return rate control. This cannot be assured for station IZ1L, since it only features a marginal amount of data points. Nevertheless, applied return rate control is assumed, since it states it in the log file and BeaconC is most likely to yield a strong returned signal.

In Figure 5.6 the median derived values for the satellite Starlette (left) can be seen. It orbits Earth on an elliptical orbit, with altitudes ranging from 800 km to 1100 km. A comparable target is the satellite Stella, shown on the right. Both satellites are designed identical, however, Stella maintains on a circular orbit at an altitude of 800 km.

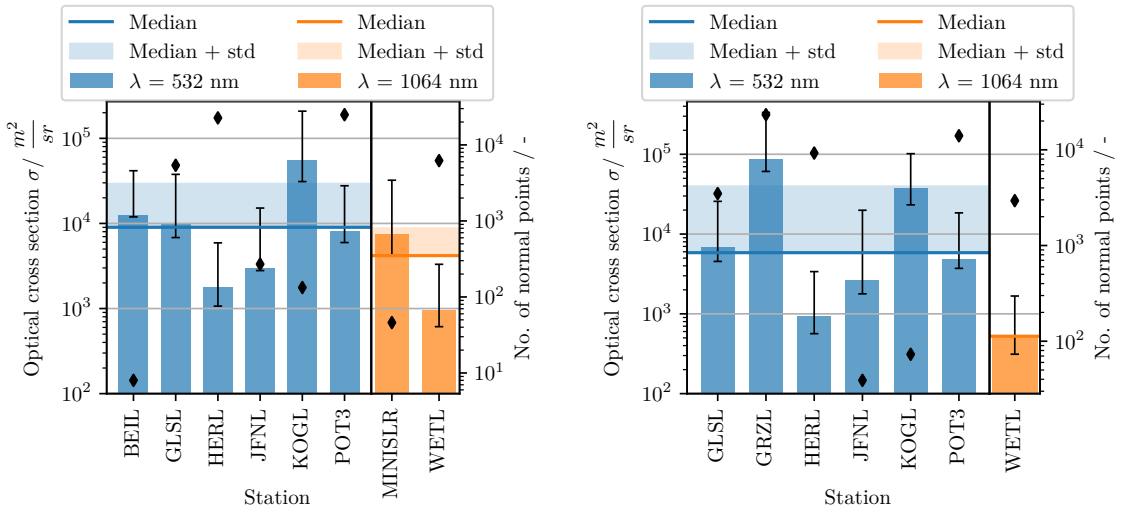

Figure 5.6: Median OCS of Starlette (left) and Stella (right), derived from the link budget of selected stations. The spherical satellites are designed identical, comprising 60 CCRs. The obtained normal points are displayed as diamonds (right axis). The data comprises measurements from 2009-01-23 to 2022-08-16.

The stations with reasonable values for Starlette yield an OCS of roughly $10^4\,\mathrm{m}^2\,\mathrm{sr}^{-1}$. These comprise BEIL, POT3 and MINISLR, whereas KOGL exhibits a larger discrepancy to the other stations, but may still be considered, since it featured reasonable values to now.
Stella exposes similar patterns, despite that the stations BEIL and GRZL are not present. What can be definitely seen is that HERL and WETl most likely perform return rate control. The ability of return rate control is stated in their log files.

To also consider lower orbiting satellites, the two satellites SwarmA (left) and SwarmB (right) are investigated. Their results are shown in Figure 5.7. SwarmA has an orbit altitude of roughly 460 km, whereas SwarmB of roughly 500 km.

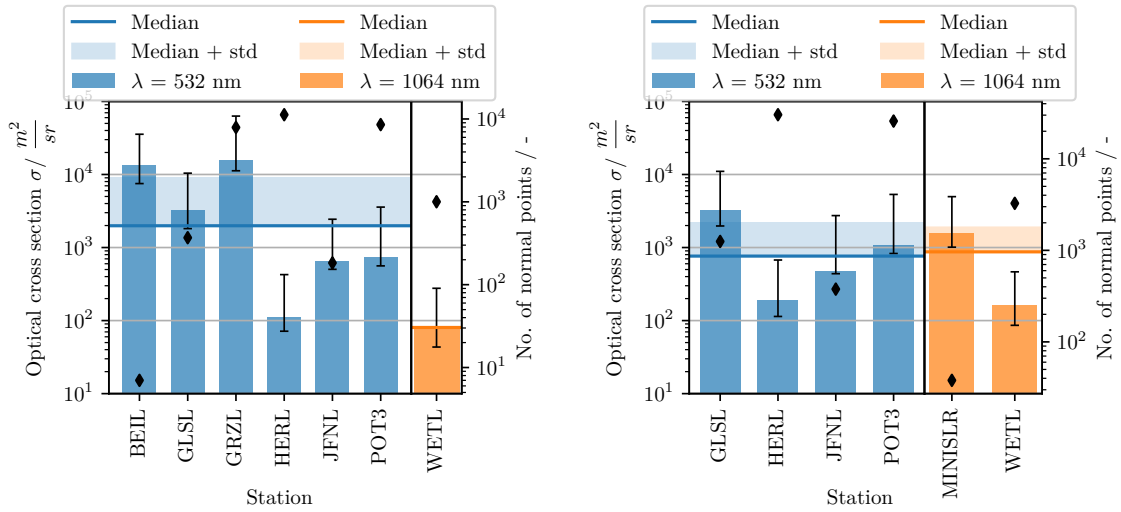

Figure 5.7: Median OCS of SwarmA (left) and SwarmB (right), derived from the link budget for selected stations. The obtained normal points are displayed as diamonds (right axis).

What stands out in the figure is that POT3 features much lower values than BEIL and GLSL and therefore is considered as invalid. Most likely originating from applied return rate control. The same is apparent for HERL, JFNL and WETL.

In conclusion, the investigated LEO satellites show that several stations exhibit larger discrepancies and a dynamical behaviour towards lower OCSs, compared to the GNSS satellites. This occurrence either stems from applied return rate control or even larger tracking or pointing losses. It greatly depends on the satellite's altitude and the equipped CCR array and cannot be assumed to be the same for all LEO satellites. Stations which most likely fall into this category are HERL and WETL. The Stations JFNL and POT3 on the other hand show only partially large discrepancies. From the station log files, it is known that JFNL does not consider return rate control. Therefore, it can be assumed that this station features larger pointing or tacking uncertainties in reality. It is known that HERL and POT3 perform return rate control, which has been clearly seen for station HERL. For POT3, barely any larger discrepancies are evident, which have only been apparent for SwarmB. Therefore, it is assumed that POT3 might not provide reliable data for the remaining satellites. Station GRZL on the other hand states in the log file that return rate control can be applied. This is not evident in the resulting OCSs so far. Moreover, the station yields quantitatively large values. Consequently, a previous distinction between the application of return rate control would not have to yield a clear outcome.
It can be concluded that the only stations that resolve reliable and reasonable values for LEO satellites are BEIL, GLSL, GRZL and KOGL for the wavelength of 532 nm and the miniSLR for 1064 nm.

In Table 5.1 the outcome of the evaluation is summarised. It lists the individual stations and if reasonable values were obtained for the investigated satellites or not. Keeping in mind that a first selection was considered after the evaluation of the Etalon and GNSS

satellites, wherefore barely any stations are present for LEO satellites. The symbols in the table indicate the following outcome:

- ✓: station yields reasonable values
- + : station yields greater values
- - : station yields lower values
- -/- : no data is present for this station

Table 5.1: Quantitative evaluation of the stations for the investigated satellites. The + indicates that the station yields large values, the - indicates low values, the ✓indicates reasonable values and -/- means that the station does not comprise data for this satellite. The green colour code represents stations that yields reasonable values for all of the investigated targets and the yellow code indicates reasonable values for MEO satellites.

Station	Lageos	Etalon + GNSS	Ajisai	BeaconC	Starlette	Swarm
AREL	-	-/-	-/-	-/-	-/-	-/-
BEIL	✓	✓	(-)	✓	✓	✓
GLSL	✓	✓	✓	✓	✓	✓
GRSM	-	-	-/-	-/-	-/-	-/-
GRZL	✓	✓	✓	-/-	-/-	-/-
HA4T	-	-/-	-/-	-/-	-/-	-/-
HERL	✓	✓	-	-	-	-
JFNL	-	✓	-	-	-	-
KOGC	✓	+	-/-	-/-	-/-	-/-
KOGL	✓	-/-	✓	✓	✓	✓
KTZL	-	-	-/-	-/-	-/-	-/-
KUN2	+	+	-/-	-/-	-/-	-/-
KUNL	-	-	-/-	-/-	-/-	-/-
MONL	-/-	-	- /-	-/-	-/-	-/-
POT3	✓	✓	✓	✓	✓	-
SFEL	-	-/-	-/-	-/-	-/-	-/-
SHA2	+	+	-/-	-/-	-/-	-/-
SIML	-	-	-/-	-/-	-/-	-/-
SJUL	-	-	-/-	-/-	-/-	-/-
STAL	-/-	-/-	-/-	-/-	-/-	-/-
STL3	-	-	- /-	-/-	-/-	-/-
THTF	+	-/-	-/-	-/-	-/-	-/-
THTL	-	-	-/-	-/-	-/-	-/-
ZIML	-	-	-/-	-/-	-/-	-/-
IZ1L	-	✓	-/-	-	-/-	-/-
MINISLR	✓	✓	✓	✓	✓	✓
UROL	+	+	-/-	-/-	-/-	-/-
WETL	✓	✓	-	-	-	-

It shows that it cannot be assured that all the stations yield reasonable values. Notice that station STAL is not apparent in any of the investigated satellites. This is because the station is declared as an engineering station [20], and consequently provides barely any data.
Considering all the investigated satellites, only five stations provide reliable data, which are marked in green in Table 5.1. In particular, for the wavelength of 1064 nm, for which it can be assumed that the miniSLR solely yields consistent and reliable values. Consequently, the miniSLR can be a valuable tool for the determination of the satellites OCSs for this particular wavelength. However, this also leads to the fact that the values of LEO satellites for the wavelength of 1064 nm cannot be validated by other stations and a bias may occur, if the specifications of the system are not completely correct. Nonetheless, it was shown that the miniSLR yields values close to the ones of station WETL for Lageos and Etalon, which can be a first indication that the miniSLR specifications are plausible. For higher orbiting satellites, such as Lageos, Etalon and GNSS satellites it has been shown that three additional stations provide reliable data, in particular HERL, POT3 and WETL, which are marked in yellow. To maximise the output of the evaluation, these stations are additionally considered for MEO and GEO satellites. Since data for the wavelength of 1064 nm is rare, the station IZ1L is further considered for MEO and GEO satellites, but excluded for Lageos. Further satellites could be investigated, but most likely would not yield any new insights, since most of the orbit altitudes and common targets have been considered.

Overall, the conducted evaluation shows that out of the 28 stations that operate at single photon levels, only a small number remain. Nevertheless, these seem to provide reliable and consistent data. The others either state incorrect system specifications, perform return rate control, or feature larger tracking uncertainties.

5.2 Satellites optical cross sections

The previous section has outlined which stations provide appropriate and consistent values for the OCS of a selection of satellites. These stations are now used to determine the OCS of the remaining satellites within the data. It was shown that only a few stations yield consistent and reasonable results. This remains true for LEO satellites and for the wavelength of 1064 nm, albeit to a smaller extent. Therefore, the values for LEO satellites should be taken with caution, especially for the wavelength of 1064 nm. Figure 3.2 showed that only a few satellites have been extensively measured with the miniSLR. Regardless of this, all available data from the miniSLR is used to get a first estimate of the satellites.

In total, the OCSs of 76 satellites and GNSS constellations was obtained. However,values for both wavelengths were not derived for all satellites. The wavelength of 532 nm comprises 65 satellites and the wavelength of 1064 nm in total 34. The latter comprises the LEO targets, measured with the miniSLR and further MEO and GEO constellations, which have been ranged from IZ1L and WETL. The GNSS targets comprise the Glonass-M, CompassI, Galileo1, Galileo2, IRNSS1, and QZSS constellations. Like before, the satellites of each GNSS constellation that feature the same CCR array, are summarised.
In order to achieve an overall value for each satellite, the derived OCSs of the selected stations are summarised to a single median value. The median is addressed again, since

major outliers can bias the mean, which may results from scarce data of single stations. As an indication of the variance, the lower 25 % and upper 75 % quantile are included. Figure 5.8 shows the satellites OCSs with variances over their mean orbit altitude. The values are derived from the stations that were declared as reliable (see Table 5.1). For better clarity, a selection of common satellites are displayed in the zoomed areas of Figure 5.8, along with the theoretical derived values. The reader is referred to Table A.2 in Chapter A.2, which comprises the outcome of the 76 satellites.

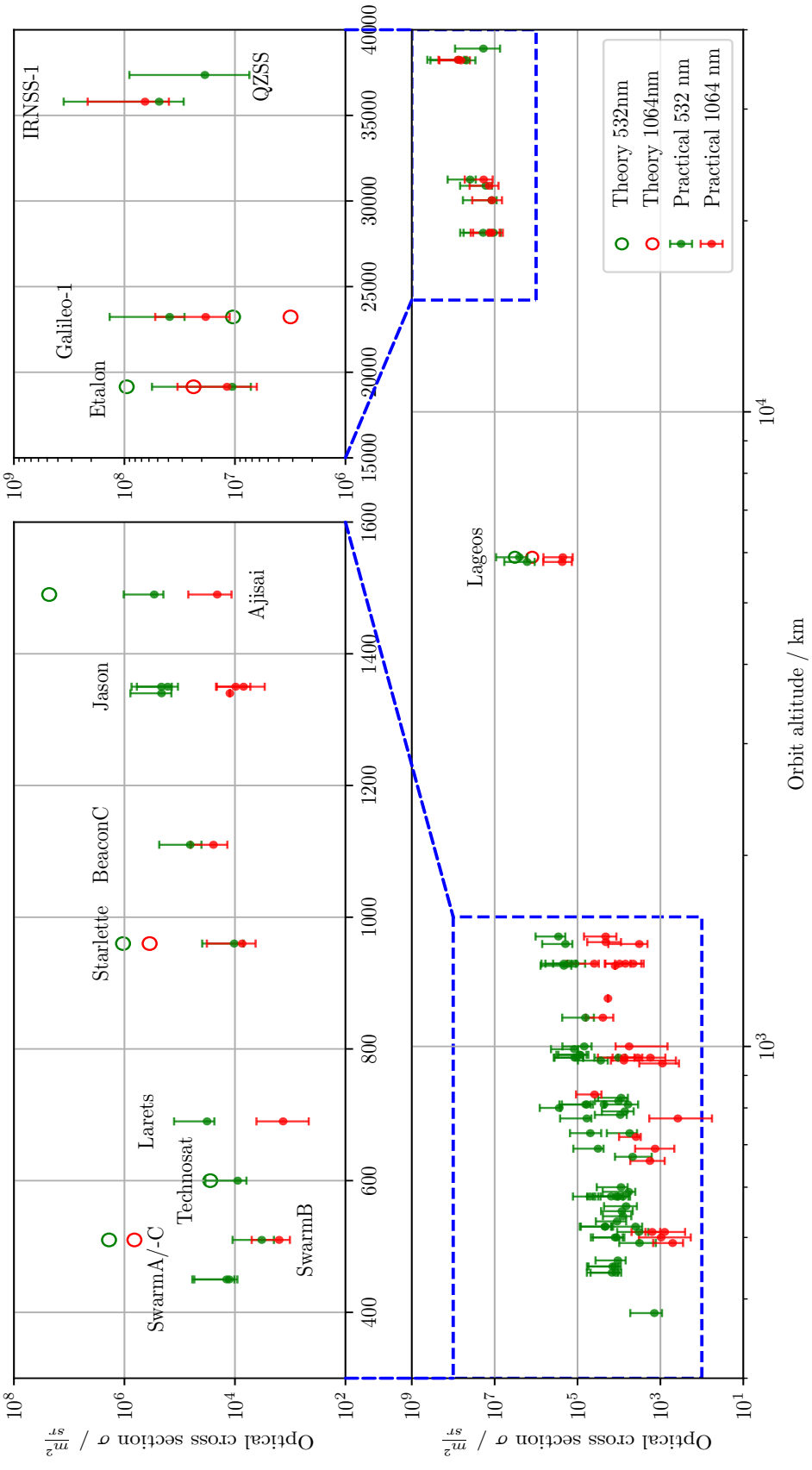

Figure 5.8: From the SLR measurements derived median OCSs over the orbit altitude. The zoomed areas show a selection of interesting targets. The error bars indicate the lower 25 % and upper 75 % quantile of the distribution. Further, theoretical values, which have been obtained by the method described in Chapter 2.5 are displayed.

What can be seen is that the trend towards greater OCSs with greater orbit altitudes is apparent. This is expected, since the decrease of the returned signal, due to large distances, has to be compromised by a large OCS. Surprisingly though, QZSS features a lower OCS than IRNSS-1, even though QZSS exhibits 56 CCRs, while IRNSS-1 has only 40 and furthermore a smaller diameter [20]. Additionally, it can be seen that the relative discrepancies among the two wavelengths are in general smaller for MEO than for LEO satellites. The latter shows a variation of one order of magnitude, whereas the high orbiting satellites remain in the same order of magnitude. This might be, because the station WETL is the main contributor to the wavelength of 1064 nm, for which it showed higher values than some of the stations utilising 532 nm.
Moreover, it is apparent that the distribution can yield lower and upper quantiles that are up to one order of magnitude apart, which can mainly be attributed to the evident values of the different stations contributing to the distribution. However, further effects can also influence the results, such as variations of weather conditions, tracking uncertainties, or the angle of incidence with respect to the CCRs.

Moving now explicit to LEO satellites, shows that the outcome of this method does not have to yield the same results for satellites of one constellation that feature the same array, such as Swarm and Jason. The Jason satellites do in fact show similar values, which speaks in favour of this method, but the Swarm satellite deviate by almost one order of magnitude. Despite the difference in orbit altitude, similar values are expected for all of the Swarm satellites. If in turn Figure 5.7 is considered, it can be seen that the variation can be attributed to the different stations contributing to the data. In the case of SwarmB, only GLSL contributes to the value, whereas for SwarmA, BEIL and GRZL are apparent. In both cases GLSL exhibits rather low values, which is compensated by the other stations in the case of SwarmA.

Turning now to the theoretical values shows that these are reflected in practice to some extent, which can be seen for Lageos-1 and Etalon. To recap the outcome of Galileo-1, it should be mentioned that a theoretical value of roughly $80 \times 10^6\,\mathrm{m^2\,sr^{-1}}$ was expected, due to the similarity to Glonass-M. The theoretical value seems unreasonably low, which is confirmed by the outcome of the link budget. Assuming that the theoretical values are upper achievable limits, exposes that in practice, an OCS of half an order of magnitude above is achieved. Consequently, the derivations of the stated theoretical model can be considered as implausible, which has been expected. Glonass-M is for better overview not included in the figure, but features a similar outcome as Etalon. The comparison of the theoretical values to the ones derived by from the measurements are summarised in Table A.3 in Chapter A.2.
The LEO satellites reveal that the theoretical values may differ by up to two orders of magnitude to the values derived from the measurements. For SwarmB this is even larger and can achieve three orders of magnitude.
But since the relative error of Etalon between theory and practice (≈ 8) is much smaller than the errors of the LEO satellites (up to 200), this might indicate that the stations feature larger tracking or pointing errors for low orbiting satellites. This most likely occurs due to the large relative velocities near zenith, but also the wide velocity aberration annulus may cause larger deviations, which is not fully compensated by the reflector design.
Moving on to Technosat, reveals that that the practical achievable value yields an OCS close to the ones of SwarmA/-C. Technosat does in fact feature smaller CCRs, but has

a large amount of CCRs that can contribute to the received signal. Since the theoretical calculation only considers one CCR, it can be assumed that the theoretical value is underestimated, taking the various discrepancies of the LEO satellites into account.
What should be emphasised is that these results greatly depend on the stations that have been selected in the previous section. It has been shown that some station do in fact yield larger values, which have been declared as invalid. The outcome of this evaluation might differ if these stations are included into the derivations.

In order to gain at least some insight of the OCS along the elevation angles, these are displayed for Etalon and Starlette in Figure 5.9. The displayed data results from the stations BEIL and GLSL, which both showed reasonable values for the two satellites. Notice that the OCS is normalised by the maximum value.

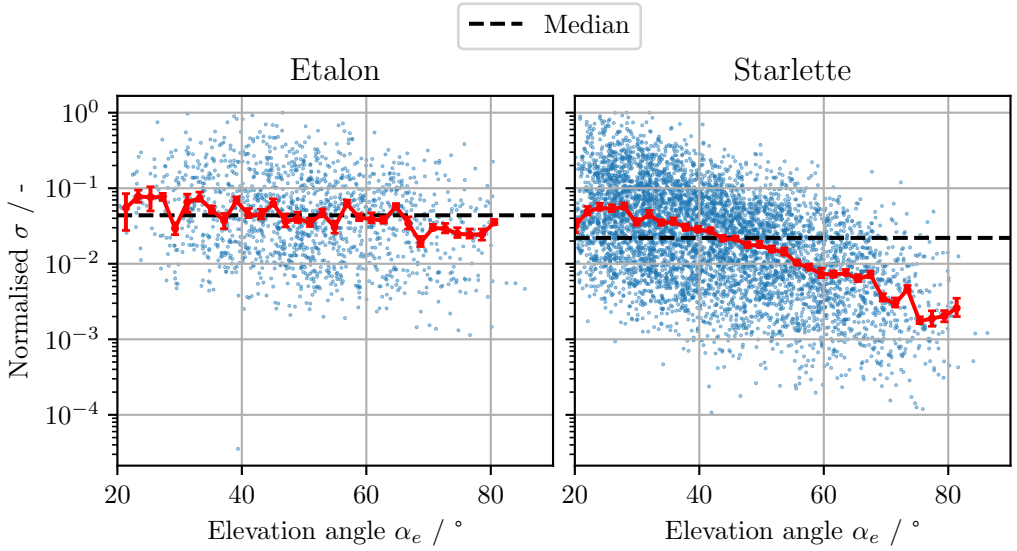

Figure 5.9: By the maximum normalised OCS over the elevation angle for Etalon (left) and Starlette (right). The data comprises the stations BEIL and GLSL.

Etalon is a high orbiting satellite, wherefore the velocity aberration annulus is small and therefore the variation of the OCS along the elevation lingers along the median. It is also known that due to the spherical shape of the satellite, the angle of incidence should not have large influence on the OCS as Degnan proposes [4].
For Starlette on the other side, it can be seen that the values trend to lower OCSs for increasing elevation angles. This may result from the larger velocity aberration annulus, but also the larger relative velocities near zenith, which challenge the tracking of the system. Again, this satellite is spherical and the angle of incidence should not have large influence. It shows though that the decrease of the OCS is due to this effect rater low, since most of the data is located at lower elevation angles. The OCS exhibits at lower elevation angles larger values, wherefore the decrease of the median is marginal. Consequently, the large discrepancies towards the theoretical values can not fully be outlined, but may be attributed to general greater tracking uncertainties.

In conclusion of this section it can be stated the that applied link budget can in fact yield reasonable OCSs, which are apparent for MEO satellites and can be validated to

some extent by the theoretical values. For LEO satellites the model seems to feature some flaws regarding the tracking uncertainties, wherefore the values cannot be validated to a full extent. But since these uncertainties can be highly dynamical and due to the limitations of the available data, these could not be considered in the course of this work. In consequence these should be considered as lower limits. Nevertheless, the obtained values can be give valuable insights on the achievable signal for several satellites and satellite groups.

5.3 Signal estimation miniSLR

Lastly, the utilised model to derive the OCSs of the individual satellites is further exploited to determine the returned signal strength of satellites, which have not been able to be ranged with the miniSLR to date. Since the variations of the derived OCS are large, the slant range to the target can be estimated via Equation 2.5. Therefore, the Earth radius at the stations location is estimated via the WGS84 model by the geodetic coordinates. The satellites orbit altitude is taken from Table A.2, which results from the mean of the orbit propagation. For high orbiting satellites, such as MEO targets, this should remain fairly constant over time.
Interesting targets are for example the Galileo-1 satellites and Lares2. The latter has been launched in the period of this work, on the 13th of Juli 2022 [45]. However, some data could be obtained for this satellite, which enabled the computation of the OCS.
Likewise the Lageos satellites it is spherical and exploited for space geodesy, but features a lesser amount and smaller CCRs. It further remains on a similar orbit as the Lageos.

Moreover, in the course of this thesis a new laser is being tested and installed into the miniSLR. The laser will presumable exhibit a pulse energy of roughly 100 µJ and a repetition rate of up to 50 kH. Theses values are utilised for the signal estimation of the two satellites, in order to investigate, if a detectable signal is achievable. The return rate and return frequency over the elevation angle for both satellites can be seen in Figure 5.10.

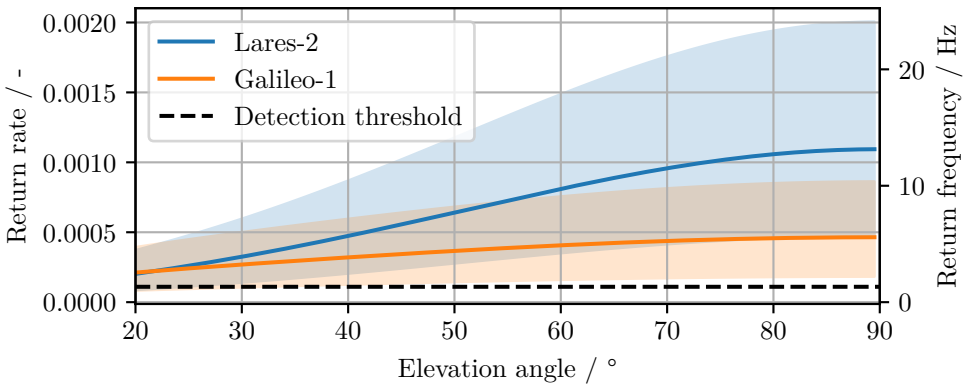

Figure 5.10: Signal estimation for the miniSLR, utilising the derived values from Table A.2 for Lares2 and Galileo-1. The coloured areas indicate the possible variances.

The utilised OCSs are therefore taken from Table A.2 in Appendix A. The coloured areas describe the possible variances that can occur. Further, the detection threshold of

the system is displayed. It results from the return rate achieved from the observation of Etalon2, which is shown in Figure 3.1b.
In this case the satellites signal is barely distinguishable from the background noise, wherefore it can be assumed that this is the minimal resolvable signal. Consequently, it is declared as the detection threshold. The resulting threshold yields a mean return rate value of 0.0011 %. In the figure it can be seen that both satellites should return a strong enough signal to be detected, even for low elevation angles. Since these targets were not able to be ranged to date, this might indicate that the system features larger pointing or tracking uncertainties in general.

6 Conclusion and outlook

This work addressed the goal of determining the OCS of satellites from available and self conducted SLR measurements. These can be valuable parameters for the signal estimation of new ground segments. Further, these derived values can give insight of the OCS for new launched satellites equipped with retroreflectors.
For this purpose, measurements from a large number of SLR stations were collected to avoid possible systematic errors that may occur from the consideration of single stations. These include the stations integrated in the ILRS network and the DLR stations, the miniSLR, and UROL. In order to consolidate the large amount of measurements, a tool was developed that maintains the data in a rational database.
From the normal points of the SLR measurements, which contain the information regarding the signal strength per pulse, the OCS has been resolved by means of a link budget model. In term of generalisation and lack of information, provided by the stations, this study is limited insofar as not all occurring losses can be taken into account. Assumptions about the atmospheric visibility had to be made, having an influence on the atmospheric transmission. Further uncertainties comprise atmospheric turbulence and background noise, which are neglected.

Nevertheless, before applying the link budget to the collected SLR measurements, the stations had to be filtered for single photon data, based on the applied system parameters and observed satellites. This is a necessary step because only for the expectation of a maximum of one detected photon per beam, the distribution of the measured signal is known and thus the average number of photons per beam can be determined. It has been shown that most of the present stations passed the filtering and remained in the data.
In order to eliminate systematic errors of individual stations, a method has been proposed to identify stations that yield reasonable OCSs. Therefore, the stations have been evaluated among a selection of common ranged satellites. It showed that a large amount of stations yield unreasonable values, which might indicate incorrect stated system specifications, which is also true for the DLR system UROL.
Some of the stations showed minor discrepancies, which can be attributed to the applied return rate control or larger tracking errors. Stations that apply return rate control are not considered in the evaluation, since the attenuation of the signal is unknown and would bias the outcome. The findings of the evaluation show that less than 10 from the almost 30 single photon operating stations provide reliable and consistent data.
Especially for LEO satellites it has been shown that barely any stations remain in the single photon level without return rate control or even larger tracking errors, in total five. Here, the miniSLR is the only station that can be assumed to provide plausible and reliable values among all LEO satellites for the wavelength of 1064 nm. Therefore, the miniSLR can be a valuable tool for future studies.
If the attenuation of the preforming return rate is recorded or known in the future, a more extensive analysis can be conducted and a larger amount of stations can be considered for these targets. Despite the limitations of the model, the study contributes to the identifi-

cation of stations that should review their system specifications, which are stated in the CRD or log files.
The stations that are declared as reliable are then employed for the determination of the OCS for the satellites remaining in the data. Hereby, larger constellations that exhibit the same CCR array are summarised, since it can be assumed that these remain on similar orbit altitudes. In total, the OCS of 76 satellites, including several GNSS constellations, have been obtained. A limitation are the LEO satellites and the wavelength of 1064 nm, because only the miniSLR contributes to the values.

Moreover, in order to evaluate the outcome of the link budget model, theoretical values of several satellites have been taken into account. A simplified approach has been implemented to determine the theoretical OCS, based on the reflector specifications and the orbit altitude. To some extend, these values have been validated successfully against available literature values, which were computed via diffraction theory. This approach yields reasonable values for most of the utilised array types, but yields larger discrepancies towards arrays, which feature uncoated TIR CCRs and small dihedral offsets.
The comparison of the values resulting from the link budget to the theoretical ones, reveals that these can vary by more than two orders of magnitude, which is in particular apparent for LEO satellites. These discrepancies can most likely be attributed to the reason that the theoretical values have to be considered as upper achievable limits and due to the limitations of the link budget model. It can be assumed that the large uncertainties for LEO satellites may be the result of larger tracking errors, which can be assigned to the large relative velocities near zenith. These uncertainties can be highly dynamical and are unknown from the provided data. For this reason, the derived OCSs are to be considered with caution and as lower achievable limits. Nevertheless, it showed that for higher orbiting satellites plausible and reasonable values are obtained and could be to some extent validated, which testifies this method.
In consequence, the derivations of this study show that the applied link budget model cannot be validated for all satellite types due to the limitations of the available data, but can give a first estimate of the achievable OCS. Nevertheless, this work provides a fundamental basis for further studies using the link budget. A further study could assess the values obtained in this study through the extension of the link budget model by further uncertainties, such as the atmospheric turbulence and the tracking or pointing errors. This should be conducted for a single SLR station, for which all the system parameters are known to a vast extent, such as the miniSLR.

In summary, this work has achieved a first approach to determine the OCS of individual satellites and constellations by the application of the link budget, taking several stations into account. However, the model used within this study still features some uncertainties and assumptions, which can be reduced by further studies in the future. Nevertheless, this work offers a first insight into the effects that need to be taken into account for the determination of an accurate link budget.

Bibliography

[1] SpaceNews. URL: https://spacenews.com/from-space-traffic-awareness-to-space-traffic-management/ (visited on 09/10/2022).

[2] Daniel Hampf et al. "MiniSLR: a fully automated miniature satellite laser ranging ground station". In: *Proceedings of the International Astronautical Congress, IAC*. 2018.

[3] Matthew Wilkinson et al. "The next generation of satellite laser ranging systems". In: *Journal of Geodesy* 93.11 (2019), pp. 2227–2247.

[4] John J Degnan. "Millimeter accuracy satellite laser ranging: a review". In: *Contributions of space geodesy to geodynamics: technology* 25 (1993), pp. 133–162.

[5] David A Arnold. *Method of calculating retroreflector-array transfer functions*. Tech. rep. 1978.

[6] John J Degnan. "A tutorial on retroreflectors and arrays for SLR". In: *International Technical Laser Workshop*. 2012.

[7] Ludwig Combrinck. "Satellite Laser Ranging". In: Jan. 2010, pp. 301–338. ISBN: SBN 978-3-642-11741-1. DOI: 10.1007/978-3-642-11741-1_9.

[8] Michael R Pearlman et al. "The ILRS: approaching 20 years and planning for the future". In: *Journal of Geodesy* 93.11 (2019), pp. 2161–2180.

[9] Felicitas Nieblera et al. "Compact Ground Station for Satellite Laser Ranging and Identification". In: *Proceedings of the International Astronautical Congress, IAC*. 2022.

[10] Daniel Hampf et al. "A path towards low-cost, high-accuracy orbital object monitoring". In: (2021).

[11] Daniel Hampf, Fabian Sproll, and Thomas Hasenohr. "OOOS: A hardware-independent SLR control system". In: (2017).

[12] Mazin Ali Abd Ali and Miami Abdulatteef Mohammed. "Effect of atmospheric attenuation on laser communications for visible and infrared wavelengths". In: *Al-Nahrain Journal of Science* 16.3 (2013), pp. 133–140.

[13] M Naboulsi, H Sizun, and F Fornel. "Propagation of optical and infrared waves in the atmosphere". In: *Proceedings of the union radio scientifique internationale* (2005).

[14] Robert Michael Pierce, Jaya Ramaprasad, and Eric C Eisenberg. "Optical attenuation in fog and clouds". In: *Optical Wireless Communications IV*. Vol. 4530. SPIE. 2001, pp. 58–71.

[15] Glenn R. Elion. "Electro-Optics Handbook". In: 1979.

[16] José Rodríguez et al. "Assessing and enforcing single-photon returns: Poisson filtering". In: *20th international workshop on laser ranging. Potsdam, Germany*. 2016. URL: https://cddis.nasa.gov/lw20/docs/2016/papers/45-Poisson_paper.pdf .

[17] Dariusz Strugarek et al. “Detector-specific issues in Satellite Laser Ranging to Swarm-A/B/C satellites”. In: *Measurement* 182 (2021), p. 109786.

[18] John J Degnan. “A data processing approach to high precision, high return rate kHz SLR stations”. In: *Proceedings of the 21th International Workshop on Laser Ranging Instrumentation*. 2018.

[19] J Degnan. “Challenges to achieving millimeter accuracy normal points in conventional multiphoton and kHz single photon SLR systems”. In: *Proceedings of the 2017 ILRS Technical workshop*. 2017.

[20] ILRS. URL: `https://ilrs.gsfc.nasa.gov/index.html` (visited on 08/08/2022).

[21] ILRS. URL: `https://ilrs.gsfc.nasa.gov/data_and_products/data/npt/index.html` (visited on 08/18/2022).

[22] ILRS. URL: `https://ilrs.gsfc.nasa.gov/data_and_products/data/npt/npt_algorithm.html` (visited on 08/18/2022).

[23] Zhou Hui et al. “Far-field diffraction pattern of a nonideal retroreflector for polarized light with an oblique incidence”. In: *Applied Optics* 59.8 (2020), pp. 2621–2631.

[24] *Corner Cube Prisms*. RP Photonics. URL: `https://www.rp-photonics.com/corner_cube_prisms.html` (visited on 07/13/2022).

[25] Philip C Stephenson. *Satellite laser ranging photon-budget calculations for a single satellite cornercube retroreflector: attitude control tolerance*. Tech. rep. DEFENCE SCIENCE and TECHNOLOGY GROUP EDINBURGH (AUSTRALIA), 2006.

[26] Daniel R. Cremons et al. “Optical characterization of laser retroreflector arrays for lunarlanders”. In: *Appl. Opt.* 59.16 (June 2020), pp. 5020–5031. DOI: `10.1364/AO.388371`. URL: `http://opg.optica.org/ao/abstract.cfm?URI=ao-59-16-5020`.

[27] Nils Bartels et al. “Design and qualification of a recessed satellite cornercube retroreflector for ground-based attitude verification via satellite laser ranging”. In: *CEAS Space Journal* 11.4 (2019), pp. 391–403.

[28] Michael A Steindorfer et al. “Attitude determination of Galileo satellites using high-resolution kHz SLR”. In: *Journal of Geodesy* 93.10 (2019), pp. 1845–1851.

[29] M Pearlman et al. “Laser geodetic satellites: a high-accuracy scientific tool”. In: *Journal of Geodesy* 93.11 (2019), pp. 2181–2194.

[30] Daniel Hampf et al. “Satellite laser ranging at 100 kHz pulse repetition rate”. In: *CEAS Space Journal* 11.4 (2019), pp. 363–370.

[31] International Laser Ranging Service. URL: `https://ilrs.gsfc.nasa.gov/data_and_products/formats/crd.html/` (visited on 08/08/2022).

[32] NASA. URL: `https://earthobservatory.nasa.gov/features/OrbitsCatalog` (visited on 08/20/2022).

[33] JPL. URL: `https://sealevel.jpl.nasa.gov/missions/topex-poseidon/summary/` (visited on 10/22/2022).

[34] *JenLas fiber ns*. 040401-041-98-0212. Rev. 2. JENOPTIK Laser GmbH. Aug. 2014.

[35] EUROLAS Data Center. URL: `https://edc.dgfi.tum.de/en/` (visited on 08/08/2022).

[36] David A Arnold. “Cross section of ILRS satellites”. In: *ILRS Technical Workshop*. 2003, pp. 1–7.

[37] URL: https://refractiveindex.info/?shelf=glass&book=fused_silica&page=Malitson (visited on 10/20/2022).

[38] *Galileo: Reflector Information*. ILRS. URL: https://ilrs.gsfc.nasa.gov/missions/satellite_missions/current_missions/ga06_reflector.html (visited on 07/13/2022).

[39] Ludwig Grunwaldt, Reinhart Neubert, and Merlin F Barschke. "Optical tests of a large number of small COTS cubes". In: *20th International Workshop on Laser Ranging*. 2016.

[40] Meng Wendong et al. "Research on Technology of 1064nm SLR and Preliminary Measurement Experiment". In: ().

[41] URL: https://www.space-track.org/ (visited on 08/20/2022).

[42] URL: hhttp://celestrak.org/ (visited on 08/20/2022).

[43] NATIONAL GEOSPATIAL-INTELLIGENCE AGENCY. URL: https://earth-info.nga.mil/index.php?dir=wgs84&action=wgs84 (visited on 08/20/2022).

[44] URL: https://rhodesmill.org/skyfield/ (visited on 08/20/2022).

[45] Spektrum. URL: https://www.spektrum.de/news/satellit-lares-2-stellt-einsteins-theorie-auf-die-probe/2044843 (visited on 09/01/2022).

[46] David A Arnold. *Optical and infrared transfer function of the LAGEOS retroreflector array*. Tech. rep. 1978.

[47] David A Arnold. *Optical transfer function of Starlette retroreflector array*. Tech. rep. 1975.

[48] Krzysztof Sośnica et al. "Satellite laser ranging to GPS and GLONASS". In: *Journal of Geodesy* 89.7 (2015), pp. 725–743.

[49] Toshimichi Otsubo, Graham M Appleby, and Philip Gibbs. "GLONASS laser ranging accuracy with satellite signature effect". In: *Surveys in geophysics* 22.5 (2001), pp. 509–516.

[50] Reinhart Neubert, Ludwig Grunwaldt, and Jakob Neubert. "The retro-reflector for the CHAMP satellite: Final design and realization". In: *Proceedings of the 11th international workshop on laser ranging*. 1998, pp. 260–270.

List of Figures

List of Tables

A Appendix

Table A.1: Input parameters to the theoretical computation of the OCSs by the method proposed by Degnan [6], which is described in Chapter 2.5. The stated method is a simplification of the derivations of Arnold [5].

Satellite	D_{ccr} / mm	L_{ccr} / mm	n (532 nm / 1064 nm) / -	ρ / -	δ / $''$	n_δ / -	N_{ccr} / -	$\theta_{i,max}$ / $^\circ$	h_{sat} / km	Reference
Lageos	0.0381	0.0278	1.461 / 1.45	0.93	1.25	3	422	55	6000	[46]
Starlette	0.0328	0.0233	1.457 / 1.45	0.78	1.47	3	60	57	950	[47]
Etalon	0.0283	0.0191	1.461 / 1.45	0.93	2.4	1	2140	60	19100	[48, 49]
Glonass-M	0.0283	0.0191	1.461 / 1.45	0.93	2.4	1	112	14	19100	[48, 49]
Champ	0.038	0.028	1.461 / 1.45	0.78	3.8	1	1	55	600	[50]
Galileo-1	0.033	0.0233	1.461 / 1.45	0.93	0.8	3	84	12	23200	[38]
Galileo-2	0.0282	0.0191	1.461 / 1.45	0.93	0.8	3	60	12	23200	[38]
SwarmB	0.038	0.028	1.461 / 1.45	0.78	3.8	1	1	55	510	[50]
Technosat	0.01	0.0075	1.461 / 1.45	0.78	0	3	1	54	600	[39]

A.1 Derived OCS for several stations

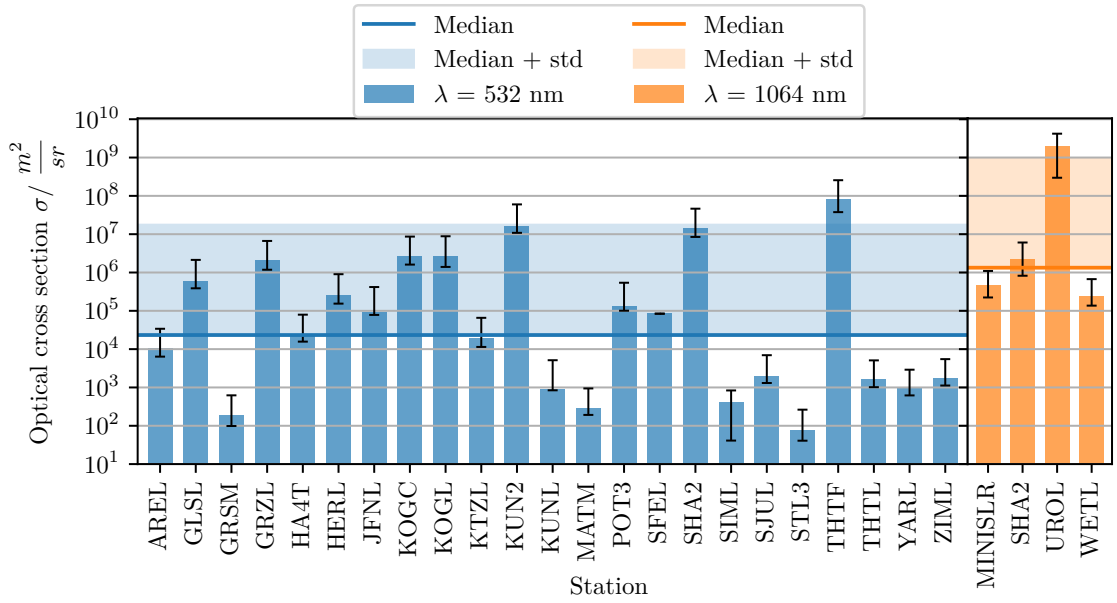

Figure A.1: Median OCS of Lageos-2, derived from the link budget of the individual stations for the wavelengths of 532 nm and 1064 nm. The data comprises measurements from 2009-07-26 to 2022-03-03.

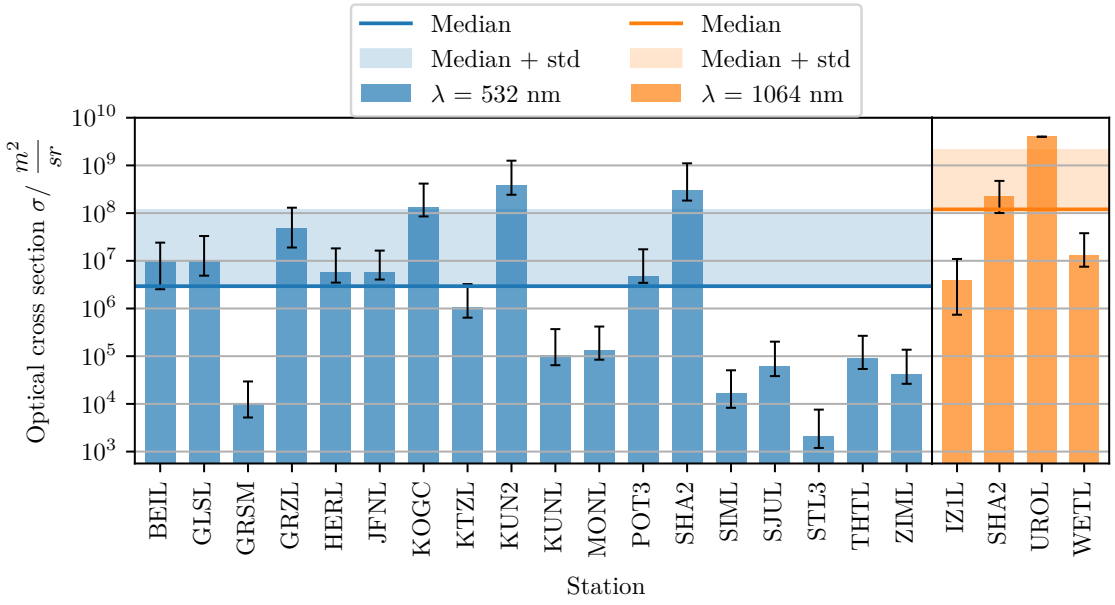

Figure A.2: Median OCS of Glonass-M satellites, derived from the link budget of the individual stations for the wavelengths of 532 nm and 1064 nm. The Glonass-M constellation comprises in total 21 satellites, which are summarised due to the fact that they exhibit the identical CCR array and feature similar orbit altitudes. The data comprises measurements from 2009-07-26 to 2022-03-03.

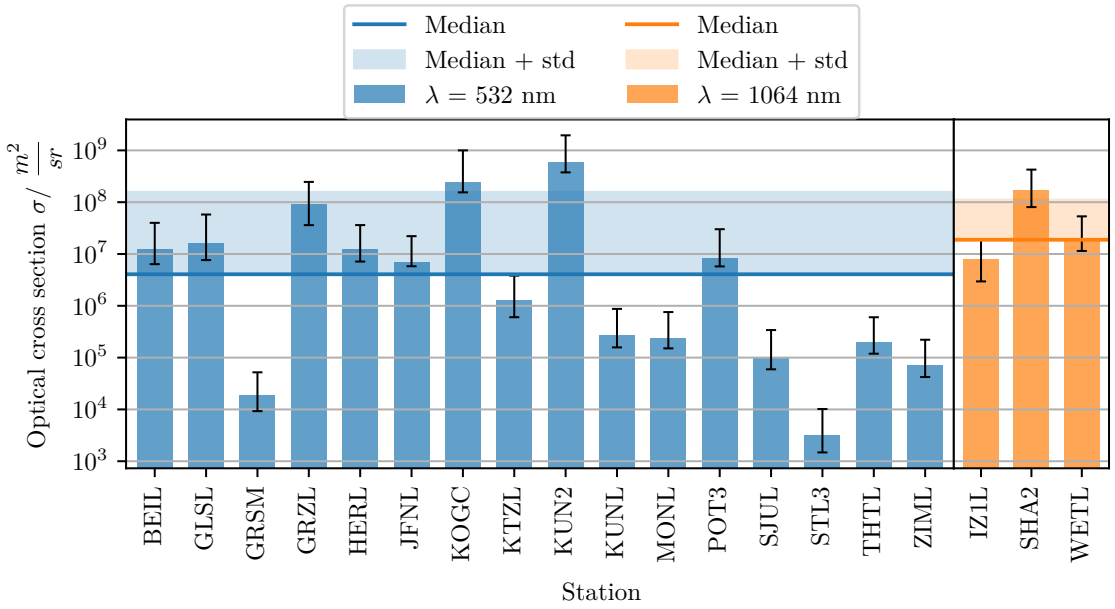

Figure A.3: Median OCS of Galileo first generation satellites, derived from the link budget of the individual stations. The constellation comprises four satellites (Galileo-101 to Galileo-104). The data comprises measurements from 2011-11-30 to 2022-08-07.

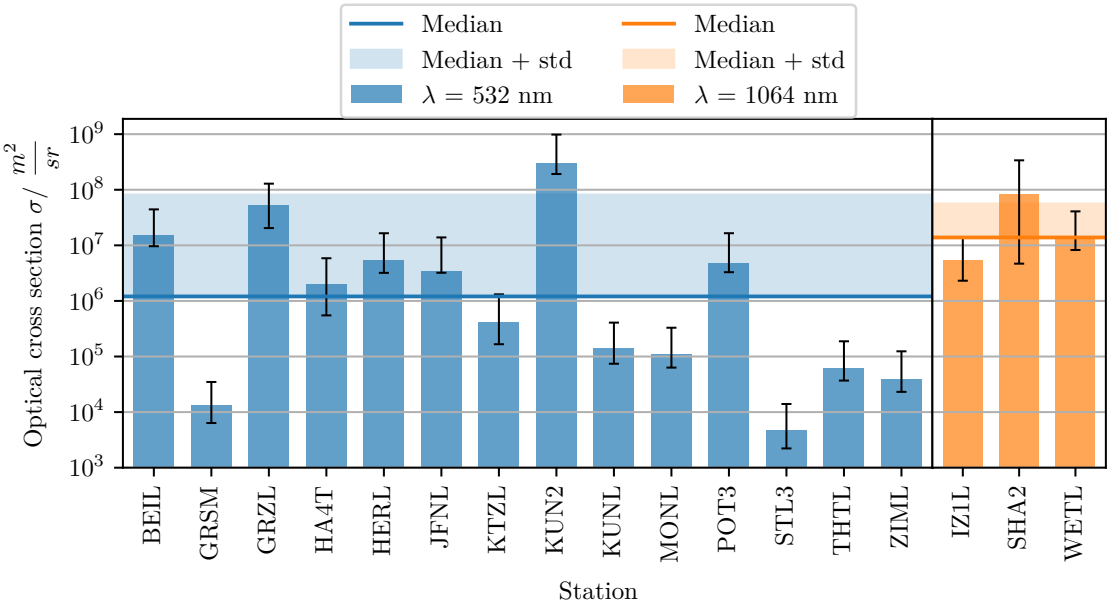

Figure A.4: Median OCS of Galileo second generation satellites, derived from the link budget of the individual stations. The constellation comprises 23 satellites (Galileo-201 to Galileo-224). The data comprises measurements from 2014-12-05 to 2022-08-07.

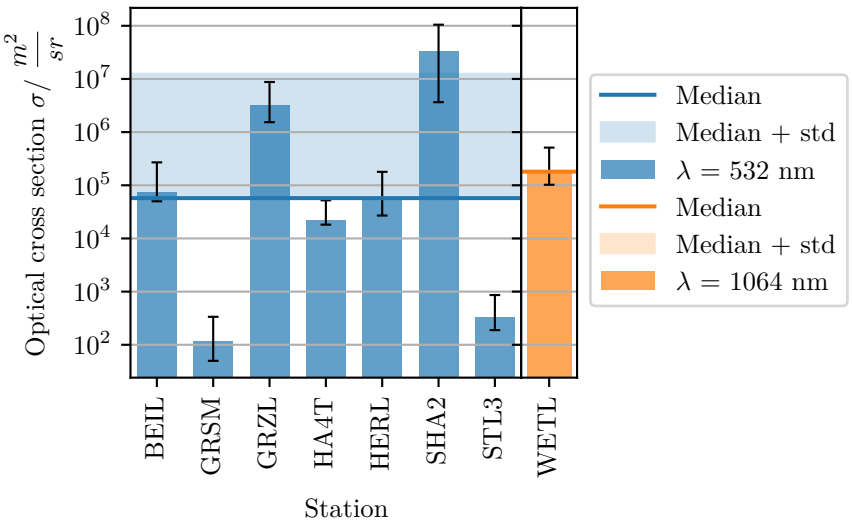

Figure A.5: Median OCS of Lares-2, derived from the link budget for selected stations.

A.2 Derived OCS for several satellites

Table A.2: From the link budget derived OCSs for the remaining satellites in the data. he minimal and maximal values results from the lower 25 % and upper 75 % quantile, respectively. These are ordered by the mean orbit altitude h_{sat} resulting from the orbit propagation. It should be noticed that the table also contains satellites that are not in orbit anymore, therefore show low orbit altitudes, such as GOCE.

		OCS 532 nm / $m^2\,sr^{-1}$			OCS 1064 nm / $m^2\,sr^{-1}$			
NORAD ID	Satellite	Min	Median	Max	Min	Median	Max	h_{sat} / km
34602	GOCE	264	635	1219	NaN	NaN	NaN	250
35694	ANDEC	15	64	105	NaN	NaN	NaN	270
40314	SPINSAT	482	1399	3938	NaN	NaN	NaN	380
27391	GRACEA	4158	14715	44705	NaN	NaN	NaN	440
27392	GRACEB	3103	11943	36515	NaN	NaN	NaN	440
39452	SWARMA	3918	14145	44967	NaN	NaN	NaN	450
39453	SWARMC	3631	12661	41745	NaN	NaN	NaN	450
40903	PN1A	3766	10652	26120	NaN	NaN	NaN	460
41464	LOMONOSOV	1898	3195	6645	NaN	NaN	NaN	490
43613	ICESAT2	NaN	NaN	NaN	223	507	990	490
43476	GRACEFO1	4047	11469	30986	777	962	2339	500
43477	GRACEFO2	4328	12453	35129	NaN	NaN	NaN	500
39451	SWARMB	1301	3273	7761	573	1585	3387	510
38046	ZY3	NaN	NaN	NaN	535	789	1506	510
31698	TERRASARX	6484	21451	61820	NaN	NaN	NaN	520
36605	TANDEMX	6347	21850	66178	NaN	NaN	NaN	520
43215	PAZ	1224	3982	9885	NaN	NaN	NaN	520
48900	TUBIN	4413	11123	24947	NaN	NaN	NaN	530
51288	ELSADTGT	2986	8028	16374	NaN	NaN	NaN	540
47944	ELSADCHS	3849	8508	18531	NaN	NaN	NaN	550
39227	KOMPSAT5	3036	6731	16246	NaN	NaN	NaN	560
28809	OICETS	18135	49841	79131	NaN	NaN	NaN	580
43186	SNET2	4541	10472	27081	NaN	NaN	NaN	580
43187	SNET3	4928	15423	43076	NaN	NaN	NaN	580
43188	SNET4	2648	8054	19765	NaN	NaN	NaN	580
43189	SNET1	3802	11741	30125	NaN	NaN	NaN	580
43798	ASTROCSTP1	1755	5798	18901	NaN	NaN	NaN	590
42829	TECHNOSAT	2724	8914	25413	NaN	NaN	NaN	600
33496	SOHLA1	NaN	NaN	NaN	1002	1791	3533	660
25636	SUNSAT	3057	4680	7795	NaN	NaN	NaN	670
27944	LARETS	8404	31979	94305	881	1343	2735	690
28480	CZ2CR/B	NaN	NaN	NaN	886	3868	6081	720
36037	PROBA2	22311	49147	102886	NaN	NaN	NaN	730
36508	CRYOSAT2	1861	5528	14113	NaN	NaN	NaN	730
23560	ERS2	13298	59693	203718	322	379	1480	770
27386	ENVISAT	2797	9292	28954	NaN	NaN	NaN	780
39086	SARAL	2816	7238	18571	NaN	NaN	NaN	790
24277	ADEOS	20839	276334	540135	NaN	NaN	NaN	800
22824	STELLA	15839	63838	209326	NaN	NaN	NaN	810
27597	ADEOS2	22919	22919	22919	NaN	NaN	NaN	810
41335	SENTINEL3A	2607	6060	15275	NaN	NaN	NaN	810
43437	SENTINEL3B	16740	59216	178785	NaN	NaN	NaN	810

Table A.2 continued from previous page

NORAD ID	Satellite	Min	Median	Max	Min	Median	Max	h_{sat} / km
25398	WESTPAC	3651	10237	27708	NaN	NaN	NaN	820
35871	BLITS	2764	8861	23207	NaN	NaN	NaN	830
7734	GEOS3	NaN	NaN	NaN	12409	38878	69499	840
22782	METEOR22	NaN	NaN	NaN	536	893	2341	940
41579	GEOIK2	8882	27520	70462	NaN	NaN	NaN	950
20671	SL14R/B	NaN	NaN	NaN	7174	7597	8020	950
7646	STARLETTE	3299	10318	28799	3183	7411	24791	960
46469	HY2C	43868	117513	256265	987	1746	12537	960
48621	HY2D	33783	106347	252480	786	3529	7147	960
37781	HY2A	29241	89847	233755	NaN	NaN	NaN	970
43655	HY2B	30944	85798	204479	NaN	NaN	NaN	970
39068	STSAT2C	22581	119830	317251	NaN	NaN	NaN	990
27005	REFLECTOR	23132	68935	162887	NaN	NaN	NaN	1000
11327	SL8R/B	NaN	NaN	NaN	5016	5690	6365	1000
1328	BEACONC	24213	64536	169923	10736	24467	38491	1110
22969	METEOR36	NaN	NaN	NaN	18455	18455	18455	1190
33105	JASON2	71516	212808	566567	12351	12351	12351	1340
26997	JASON1	56803	164366	430664	6813	9705	11590	1350
41240	JASON3	75349	214469	529274	1718	6984	14964	1350
46984	SENTINEL6A	49317	114761	273081	2001	4538	7889	1350
22076	TOPEX	NaN	NaN	NaN	8807	39469	141441	1350
38077	LARES	62705	196041	516243	1183	3234	14840	1450
2680	DIADEME1D	NaN	NaN	NaN	11783	20716	37569	1460
16908	AJISAI	91367	288751	739684	9394	20931	48869	1490
22195	LAGEOS2	119546	343197	1190722	97272	234074	439036	5800
8820	LAGEOS1	168160	461044	1699797	95272	226301	438223	5900
53105	Lares2	28469	57350	127536	78065	180381	331022	5900
-	ETALON1/-2	3420000	10600000	45700000	5460000	11800000	21300000	19150
-	GLONASS122/-143	4710000	18900000	48900000	5650000	13200000	24600000	19150
-	COMPASSM	2720000	11700000	46600000	5050000	11700000	23000000	21550
-	GALILEO201/-224	4630000	16300000	51900000	5430000	13500000	26600000	22710
-	GALILEO101/-104	10400000	39000000	97100000	7240000	18400000	34200000	23230
-	IRNSS1	19400000	48500000	306000000	25500000	65100000	150000000	35800
-	COMPASSI	19300000	73300000	347000000	29000000	76900000	148800000	35870
-	QZSS	11300000	18700000	71500000	NaN	NaN	NaN	37360

Table A.3: Comparison of theoretical values obtained with the method stated in Chapter 2.5 and values derived from the SLR measurements via the link budget. The minimal and maximal values results from the lower 25 % and upper 75 % quantile, respectively.

Satellite	OCS / $10^6\,m^2\,sr^{-1}$ for 532 nm				OCS / $10^6\,m^2\,sr^{-1}$ for 1064 nm			
	Theoretical	Practice			Theoretical	Practice		
		Min	Median	Max		Min	Median	Max
Lageos	3.25	0.92	2.54	6.69	1.24	0.095	0.23	0.44
Glonass-M	81.6	4.71	18.9	48.9	20.6	5.65	13.2	24.6
Etalon	95.4	3.42	10.6	45.7	23.7	5.46	11.8	21.3
Ajisai	23*	0.09	0.29	0.74	-	0.009	0.021	0.049
Starlette	1.06	0.0033	0.01	0.029	0.35	0.0032	0.0074	0.025
SwarmB	1.9	0.0013	0.0033	0.0078	0.66	0.00057	0.0016	0.0034
Technosat	0.028	0.0027	0.009	0.0078	0.025	-	-	-

Table A.4: Stations of the ILRS

Monument	Code	Location Name, Country
7848	AJAF	Ajaccio, France (FTLRS)
1879	ALTL	Altay, Russia
7045	APOL	Apache Point, NM
7403	AREL	Arequipa, Peru
1886	ARKL	Arkhyz, Russia
1890	BADL	Badary, Russia
1887	BAIL	Baikonur, Kazakhstan
7357	BEIA	Beijing-A, China
7249	BEIL	Beijing, China
7343	BEIT	Beijing (TROS), China
7811	BORL	Borowiec, Poland
7407	BRAL	Brasilia, Brazil
7370	BURF	Burnie, Tasmania (FTLRS)
7548	CGLL	Cagliari, Italy
7830	CHAF	Chania, Crete, Greece
7237	CHAL	Changchun, China
7405	CONL	Concepcion, Chile
7359	DAEK	Daedeok, Republic of Korea
1824	GLSL	Golosiiv, Ukraine
7358	GMSL	Tanegashima, Japan
7130	GO4T	Greenbelt, MD
7105	GODL	Greenbelt, Maryland
7829	GRAF	Grasse, France (FTLRS)
7846	GRSF	Grasse, France (FTLRS)
7835	GRSL	Grasse, France (SLR)
7845	GRSM	Grasse, France (LLR)

7839	GRZL	Graz, Austria
7119	HA4T	Haleakala, Hawaii
7210	HALL	Haleakala, Hawaii
7501	HARL	Hartebeesthoek, South Africa
7840	HERL	Herstmonceux, United Kingdom
7831	HLWL	Helwan, Egypt
7503	HRTL	Hartebeesthoek, South Africa
1891	IRKL	Irkutsk, Russia
7701	IZ1L	Izaña (Tenerife), Spain
7396	JFNL	Wuhan, China
7335	KASL	Kashima, Japan
7308	KOGC	Koganei, Japan(CRL)
7328	KOGL	Koganei, Japan
1868	KOML	Komsomolsk-na-Amure, Russia
1893	KTZL	Katzively, Ukraine
7819	KUN2	Kunming, China
7820	KUNL	Kunming, China
7356	LHAL	Lhasa, China
7041	LLCD	White Sands,New Mexico
1831	LVIL	Lviv, Ukraine
1864	MAIL	Maidanak 1, Uzbekistan
7939	MATL	Matera, Italy (SAO)
7941	MATM	Matera, Italy (MLRO)
7080	MDOL	McDonald Observatory, Texas
1870	MDVL	Mendeleevo 1, Russia
1874	MDVS	Mendeleevo 2, Russia
7806	METL	Metsahovi, Finland
7337	MIUL	Miura, Japan
7110	MONL	Monument Peak, California
7843	ORRL	Orroral, Australia
7828	PARF	Paris, France (FTLRS)
7841	POT3	Potsdam, Germany
7836	POTL	Potsdam, Germany
1884	RIGL	Riga, Latvia
7832	RIYL	Riyadh, Saudi Arabia
7394	SEJL	Sejong City, Republic of Korea
7823	SFEF	San Fernando, Spain
7824	SFEL	San Fernando, Spain
7821	SHA2	Shanghai, China
7837	SHAL	Shanghai, China
1873	SIML	Simeiz, Ukraine
7838	SISL	Simosato, Japan
7406	SJUL	San Juan, Argentina
7827	SOSW	Wettzell, Germany
7825	STL3	Mt Stromlo, Australia
7849	STRL	Mt Stromlo, Australia
1888	SVEL	Svetloe, Russia

7339	TATL	Tateyama, Japan
7822	THTF	Tahiti
7124	THTL	Tahiti, French Polynesia
7816	UROL	Stuttgart, Germany
7355	URUL	Urumqi, China
8834	WETL	Wettzell, Germany (WLRS)
7594	WETT	Wettzell, Germany (TIGO)
7231	WUHL	Wuhan, China
7090	YARL	Yarragadee, Australia
1889	ZELL	Zelenchukskya, Russia
7810	ZIML	Zimmerwald, Switzerland

B External Data

Python code

E01	slr_data_analyis.zip

Observation data and miniSLR runs

O01	Observation_data.db
O02	Single_photon_data.db
O03	miniSLR_runs.zip